

1 **Thermo-mechanical effects of microcontinent collision**  
2 **on ocean-continent subduction system**

3 **Alessandro Regorda<sup>1</sup>, Manuel Roda<sup>1</sup>**

4 <sup>1</sup>Department of Earth Sciences, Università degli Studi di Milano, Milan, Italy

5 **Key Points:**

- 6 • The subduction dynamics is influenced by different velocities imposed on both plates  
7 in case of same overall convergent rate  
8 • Size and location of the microcontinent and convergence velocities of both plates  
9 affect the style of the subduction zone  
10 • The final thermal state inside the mantle wedge can be significantly affected by  
11 the presence and the dimension of the microcontinent

---

Corresponding author: Alessandro Regorda, [alessandro.regorda@unimi.it](mailto:alessandro.regorda@unimi.it)

## Abstract

Microcontinents are globally recognized as continental regions partially or entirely surrounded by oceanic lithosphere. Due to their positioning, they may become entangled in subduction zones and undergo either accretion or subduction. High-pressure metamorphism in subducted continental rocks support the idea that microcontinents can be subducted, regardless of their low densities. In this study, we used 2D numerical models to simulate collision of microcontinents with different sizes located at various distances from the upper plate in a subduction system characterized by different convergence velocities, in order to examine their effects on the thermo-mechanical evolution of subduction systems. Specifically, we analyzed the conditions that favor either subduction or accretion of microcontinents and investigated how their presence affects the thermal state within the mantle wedge. Our results reveal that the presence of microcontinents can lead to four styles of subduction: 1) continuous subduction; 2) continuous subduction with jump of the subduction channel; 3) interruption and restart of the subduction; 4) continental collision. We discovered that larger microcontinents and higher velocities of the subducting plate contrast a continuous subduction favoring accretion, while farther initial locations from the upper plate and higher velocities of the upper plate favor the subduction of the microcontinent. Additionally, we observed that the style of subduction has direct effects on the thermal state, with important implications for the potential metamorphic conditions recorded by subducted continental rocks. In particular, models characterized by parameters that favor the subduction of a larger amount of continental material from the microcontinent exhibit warm mantle wedges.

## Plain Language Summary

Microcontinents are fragments of continents partially or entirely surrounded by an ocean. Due to the relative motion of tectonic plates, they can either be accreted to the continental plate or subducted below it. In our study, we utilized computer simulations to investigate the conditions favoring subduction or accretion and how the presence of microcontinents varying in size and location in the ocean can impact temperatures in the subduction system. Our results reveal that the presence of a microcontinent can lead to four different styles of subduction. These styles are determined by the dimension of the microcontinent, its position in the ocean, and the velocity at which it converges toward the continent: 1) uninterrupted subduction; 2) relocation of the subduction from the front to the back of the microcontinent without interruption; 3) interruption and restart of the subduction; and 4) no subduction. We observed that higher convergence velocities and a greater initial distance between the microcontinent and the continent favor uninterrupted subduction (style 1). On the other hand, larger microcontinents and higher velocities of the ocean favor the relocation or momentary interruption of the subduction (styles 2-4). Finally, we noted that microcontinents induce noticeable changes in temperatures within the subduction system.

## 1 Introduction

The oceanic lithosphere is characterized by lithological heterogeneities that are considered to represent remnants of extinct arcs, abandoned spreading ridges (aseismic ridges), anomalous volcanic piles, uplifted oceanic crust, and sea mounts. Sometimes even submarine regions of continental crust can occur on the oceanic plate and are subdivided into continental fragments (or ribbons) or microcontinents (Scrutton, 1976; Stein & Ben-Avraham, 2007; Vogt & Gerya, 2014). The continental fragments are bound by oceanic crust on one side and thick sedimentary basins overlying extremely thinned continental crust on the other. Microcontinents, instead, are entirely surrounded by oceanic lithosphere (Scrutton, 1976; Tetreault & Buiter, 2014). Their length varies from tens to hun-

61 dreds of kilometers, with a width of 20-40 km (Tetreault & Buiter, 2014; Nemčok et al.,  
62 2016).

63 The microcontinents, in particular, can form from passive or active margins. In the  
64 first case, during rifting, continental fragments can be separated from the continental mar-  
65 gin and eventually become bounded by oceanic lithosphere. The formation of microcon-  
66 tinents at passive margins requires a combination of preexisting linear weaknesses in the  
67 continental lithosphere (van den Broek et al., 2020), rotational or oblique extension (Molnar  
68 et al., 2018), and variation in extension magnitude over time (Magni et al., 2021). The  
69 separation of microcontinents from passive margins usually occurs during the latest stages  
70 of continental breakup, before the onset of seafloor spreading (Molnar et al., 2018). How-  
71 ever, it may also occur after the onset of seafloor spreading, due to the ridge jump onto  
72 adjacent zones of weakness when the former spreading ridge becomes amagmatic (Müller  
73 et al., 2001; Péron-Pinvidic & Manatschal, 2010; Sinha et al., 2015; Abera et al., 2016).  
74 Microcontinents can form from an active margin in a subduction setting as a result of  
75 ridge jump in back-arc basins in combination with rotational or oblique extension (van den  
76 Broek & Gaina, 2020; van den Broek et al., 2020; Magni et al., 2021) or a plume-induced  
77 break-up (Koptev et al., 2019).

78 Since a microcontinent is situated on an oceanic plate, it becomes entangled in sub-  
79 duction zones, where it can be either accreted or subducted (Tetreault & Buiter, 2012,  
80 2014). Despite the relatively low density of continental crust, evidence supporting its sub-  
81 ductability emerges from numerous discoveries of high-pressure mineral associations in  
82 continental rocks (Chopin, 1984; Smith, 1984; X. Wang et al., 1989; N. V. Sobolev & Shatsky,  
83 1990; Chopin, 2003; Liu et al., 2007) and geodynamic modeling (Gerya & Stöckhert, 2006;  
84 Afonso & Zlotnik, 2011; Roda et al., 2012). This implies that lithospheric buoyancy alone  
85 is insufficient to resist subduction when considering all factors of subduction dynamics  
86 (Tetreault & Buiter, 2012). According to the analysis by Cloos (1993), the maximum  
87 thickness of subductable crustal fragments is estimated to be 15–20 km. Ellis et al. (1999)  
88 demonstrated that continental fragments measuring 30 km in thickness and 90 km in width  
89 undergo deformation and folding during subduction within the subduction channel. How-  
90 ever, these experiments did not consider the sub-lithospheric mantle, thermal evolution,  
91 or substantial convergence rates. The nature of the subduction interface also plays a role  
92 in crust subductability (De Franco et al., 2008a, 2008b).

93 Previous works have analyzed the impact of various parameters on the evolution  
94 of subduction systems characterized by oceanic plateaus, seamounts, or microcontinents  
95 (e.g. De Franco et al., 2008a; Gerya et al., 2009; Tetreault & Buiter, 2012; Vogt & Gerya,  
96 2014; Yang et al., 2018; Tao et al., 2020; Gün et al., 2022; Yan et al., 2022). However,  
97 these models typically focused on very large terranes located at significant distances ()  
98 from the initial trench, emphasizing mechanical effects such as subductibility or mate-  
99 rial recycling, with less attention to thermal effects. De Franco et al. (2008b) illustrated  
100 how a subduction channel facilitates the coherent and steady-state subduction of a con-  
101 tinental fragment, enabling subduction regardless of the geometry and strength of the  
102 incoming continental crust. In contrast, in discrete subduction faults, coherent subduc-  
103 tion of incoming continental material occurs when the colliding terrane’s continental rise  
104 is gentle. Conversely, trench locking and probable subsequent slab break-off occur if the  
105 terrane’s margin is steep and the strength of its lower crust is high. Regardless of the  
106 subduction interface nature, the strength of the incoming continental crust significantly  
107 influences the accretion or subduction of the continental fragment. A weak lower crust  
108 facilitates accretion through shear delamination of the upper crust, while a strong lower  
109 crust results in a more coherent subduction of the continental fragment (De Franco et  
110 al., 2008b; Tetreault & Buiter, 2012).

111 While the influence of different convergence rates in ocean-continent subduction  
112 systems has been analyzed in present-day settings (Jarrard, 1986; Lallemand et al., 2005),  
113 as well as through both analogue (e.g., Schellart, 2005; Heuret et al., 2007) and numer-

114 ical (e.g., Roda et al., 2010; Regorda et al., 2017; Wolf & Huisman, 2019) models, a sys-  
 115 tematic analysis of the thermal and mechanical effects of convergence rate and micro-  
 116 continent size on the dynamics of subduction systems in the case of microcontinent col-  
 117 lision is still lacking. This analysis will be particularly useful when compared with the  
 118 metamorphic evolution of the remnants of subducted and exhumed crustal rocks. For  
 119 instance, consider the continental nappes in the axial part of the Alpine chain (e.g., Sesia-  
 120 Lanzo Zone and Briançonnais nappes) that record high pressure and low temperature  
 121 (HP-LT) metamorphism. These nappes are interpreted either as microcontinents that  
 122 underwent subduction and subsequent exhumation (O’Brien et al., 2001; Rosenbaum &  
 123 Lister, 2005; Babist et al., 2006), or as fragments of the upper plate scraped off through  
 124 ablative subduction and recycled within the subduction channel (Polino et al., 1990; Spalla  
 125 et al., 1996; Gerya & Stöckhert, 2006; Roda et al., 2012) during oceanic subduction. An-  
 126 alyzing the thermal evolution induced by microcontinent subduction can provide more  
 127 insights into the interpretation of these continental nappes.

128 For this reason, our goals in the present work are: (i) to evaluate the effects of dif-  
 129 ferent velocities of both the subducting and the upper plate on subduction systems with-  
 130 out a microcontinent, in order to create reference models to which we compare the ef-  
 131 fects of the introduction of microcontinents, and (ii) to analyze the thermo-mechanical  
 132 effects induced by the collision of microcontinents of different sizes (ranging from 25 to  
 133 100 km wide) located at varying distances from the upper plate (ranging from 25 to 100  
 134 km). This analysis encompasses both the dynamics of ocean-continent subduction sys-  
 135 tems and the thermal evolution of the mantle wedge, where the burial and recycling of  
 136 crustal material usually occur. In particular, we will identify in which cases the system  
 137 is characterized either by a continuous subduction channel, by a detachment inside the  
 138 subducted microcontinent with the development of a new deep subduction channel, by  
 139 a jump of the subduction channel at surface in correspondence of the trench or by an  
 140 interruption of the subduction, in order to recognize settings that allow subduction and  
 141 exhumation of continental material and those characterized by accretion of the micro-  
 142 continent at the trench.

143 In the following sections, we first provide a brief description of the numerical code  
 144 and the model setup used in this study (Section 2). We then present the results obtained  
 145 when changing the convergence velocities in a subduction system without a microcon-  
 146 tinent, as well as in the case of microcontinent with different sizes (Section 3). Finally,  
 147 we discuss whether each change affects the mechanical evolution of the subduction sys-  
 148 tem and whether these changes influence the thermal conditions in the mantle wedge (Sec-  
 149 tion 4).

## 150 **2 Methods**

151 In this work, we model the thermo-mechanical evolution of a subduction-collision  
 152 system by means of the 2D finite element code FALCON (Regorda et al., 2023), which  
 153 relies on the parallel version of the direct MUMPS solver (Amestoy et al., 2001, 2006).  
 154 A complete description of the code and the results of all the benchmarks performed can  
 155 be found in Regorda (2022). Here, we present the main features implemented in the code.

### 156 **2.1 Numerical methods**

157 FALCON solves the mass, momentum and energy conservation equations in a 2D  
 158 Cartesian domain for an incompressible flow using the extended Boussinesq approxima-

159 tion (e.g., Christensen & Yuen, 1985; Ismail-Zadeh & Tackley, 2010), as follows:

$$\vec{\nabla} \cdot \boldsymbol{\sigma} + \rho \vec{g} = \vec{0} \quad (1)$$

$$\vec{\nabla} \cdot \vec{u} = 0 \quad (2)$$

$$\rho_0 C_p \left( \frac{\partial T}{\partial t} + \vec{u} \cdot \vec{\nabla} T \right) = \vec{\nabla} \cdot (k \vec{\nabla} T) + \rho H + 2\eta \dot{\boldsymbol{\epsilon}}(\vec{u}) : \dot{\boldsymbol{\epsilon}}(\vec{u}) - \alpha T \rho \vec{g} u_y \quad (3)$$

$$\boldsymbol{\sigma} = -p \mathbf{1} + 2\eta \dot{\boldsymbol{\epsilon}}(\vec{u}) \quad (4)$$

$$\dot{\boldsymbol{\epsilon}}(\vec{u}) = \frac{1}{2} \left( \vec{\nabla} \vec{u} + (\vec{\nabla} \vec{u})^T \right) \quad (5)$$

$$\rho(T) = \rho_0 (1 - \alpha(T - T_0)) \quad (6)$$

160 where  $\boldsymbol{\sigma}$  is the stress tensor,  $\rho$  is the density,  $\vec{g}$  is the gravitational acceleration vector,  
 161  $\vec{u}$  is the velocity,  $\rho_0$  is the reference density,  $C_p$  is the isobaric heat capacity,  $T$  is the tem-  
 162 perature,  $t$  is time,  $k$  is the thermal conductivity,  $H$  is the volumetric heat production,  
 163  $\eta$  is the (effective) viscosity,  $\dot{\boldsymbol{\epsilon}}$  is the strain rate tensor,  $\alpha$  is the thermal expansion co-  
 164 efficient, and  $p$  is the pressure.

We used  $Q_1 \times P_0$  elements (quadrilateral bilinear velocity-constant pressure; e.g., Thieulot & Bangerth, 2022) and, since they do not satisfy the Ladyzhenskaya, Babuska and Brezzi (LBB) stability condition (Donea & Huerta, 2003) and they are prone to element-wise checkerboard pressure pattern (van Zelst et al., 2022), the elemental pressure is smoothed by interpolating it onto nodes and then back onto elements and markers (Thieulot, 2014). The code implements the so-called penalty formulation for which the flow is very weakly compressible, so that Equation 2 can be replaced by

$$\vec{\nabla} \cdot \vec{u} = -\frac{p}{\lambda} \quad (7)$$

where  $\lambda$  is the penalty coefficient that has the same units as viscosity and it is required to be between 5 and 8 orders of magnitude larger than the dynamic viscosity  $\eta$ . A dimensionless coefficient  $\lambda^*$  (here fixed to  $10^6$ ) is then used so that the penalty factor is calculated for each element as  $\lambda(e) = \lambda^* \eta(e)$  (Donea & Huerta, 2003; Marotta et al., 2006; Bollino et al., 2022). This method allows us to eliminate the pressure from the momentum equation 1 resulting in:

$$\lambda \vec{\nabla} (\vec{\nabla} \cdot \vec{u}) + \vec{\nabla} \cdot \eta \left( \vec{\nabla} \vec{u} + (\vec{\nabla} \vec{u})^T \right) + \rho \vec{g} = \vec{0} \quad (8)$$

165 This equation is then solved for the velocity field, while the pressure can be recovered  
 166 as a post-processing step using Equation 7.

The time step is calculated by means of the Courant-Friedrichs-Lewy (CFL) condition (Anderson, 1995):

$$\delta t = C \min \left( \frac{h_m}{u_M}, \frac{h_m^2}{\kappa} \right) \quad (9)$$

167 with  $C$  is the dimensionless Courant number between 0 and 1,  $h_m = \min_{\Omega}(h)$  is the  
 168 dimension of the smallest element in the mesh,  $u_M = \max_{\Omega} |\vec{u}|$  is the maximum veloc-  
 169 ity in the domain,  $\kappa$  is the heat diffusion (typically around  $1 \times 10^{-6} \text{ m}^2 \text{ s}^{-1}$  in lithospheric-  
 170 scale models). The (nonlinear) mass and momentum conservation equations are then solved  
 171 at each time step  $\delta t$ , followed by the energy equation. The streamline-upwind Petrov-Galerkin  
 172 (SUPG) method is implemented in the energy equation to stabilize advection (Hughes  
 173 & Brooks, 1982; Thieulot, 2011). Materials are subsequently advected and topography  
 174 updated. Surface processes at the free surface have been implemented by means of the  
 175 software Fastscape (Braun & Willett, 2013; Cordonnier et al., 2019; Yuan, Braun, Guerit,  
 176 Rouby, & Cordonnier, 2019; Yuan, Braun, Guerit, Simon, et al., 2019).

177 Materials are tracked by means of the Particle-in-Cell method. A regularly distributed  
 178 swarm of Lagrangian markers covers the entire domain and their advection is performed  
 179 by means of a  $2^{nd}$ -order Runge-Kutta scheme in space. The interpolated velocity is then

180 corrected by means of the Conservative Velocity Interpolation (CVI; H. Wang et al., 2015).  
 181 Each marker tracks a given material type and the total number of markers in each el-  
 182 element is maintained between a minimum ( $n_{\min}$ ) and a maximum ( $n_{\max}$ ) value. Element-  
 183 tal properties, except for the viscosity, are calculated as the arithmetic average on all the  
 184 markers inside each element.

185 FALCON implements the Arbitrary Lagrangian Eulerian (ALE; Donea et al., 2004)  
 186 formulation to accommodate topography by means of free surface deformation: the sides  
 187 and bottom boundaries remain straight and the length of the domain in the  $x$ -direction  
 188 does not change (kinematic boundary conditions on these boundaries thereby imply a  
 189 flux of material through the boundary). However, the top boundary deforms using the  
 190 velocity field as it is resampled at equidistant abscissae with vertical adjustment of grid  
 191 nodes in each column at equidistant ordinates and topography is thus created (Thieulot,  
 192 2011). To avoid the drunken-sailor instability, the free surface stabilization algorithm of  
 193 Kaus et al. (2010) is implemented.

194 The viscosities for dislocation (ds) and diffusion (df) creep are given by

$$\eta_{\text{ds}} = \left( \frac{1}{A_{\text{ds}}} \right)^{\frac{1}{n_{\text{ds}}}} \dot{\epsilon}_e^{\frac{1-n_{\text{ds}}}{n_{\text{ds}}}} \exp \left( \frac{Q_{\text{ds}} + pV_{\text{ds}}}{n_{\text{ds}}RT} \right) \quad (10)$$

$$\eta_{\text{df}} = \frac{d^m}{A_{\text{df}}} \exp \left( \frac{Q_{\text{df}} + pV_{\text{df}}}{RT} \right) \quad (11)$$

(e.g., Gerya & Stöckhert, 2002; Billen & Hirth, 2007; Arredondo & Billen, 2016),  
 where  $A, n, Q, V$  are material dependent parameters.  $A$  is the pre-exponential factor,  $n$   
 is the stress exponent,  $Q$  is the activation energy,  $V$  is the activation volume,  $R$  is the  
 gas constant,  $d$  is the grain size,  $m$  is the grain size exponent and  $\dot{\epsilon}_e = \sqrt{I_2(\dot{\epsilon})}$  is the  
 effective strain rate, given as the square root of the second invariant of the strain rate  
 tensor. Note that diffusion creep is considered in the sublithospheric mantle only and  
 in this case the stress exponent is  $n = 1$ , so that the corresponding viscosity does not  
 depend on the strain rate. Since both types of viscous creep act simultaneously within  
 the lithosphere under the same deviatoric stress (Karato, 2008; Glerum et al., 2018), the  
 composite viscous creep  $\eta_{\text{cp}}$  is then calculated as the harmonic average between  $\eta_{\text{df}}$  and  
 $\eta_{\text{ds}}$  (e.g., Duretz et al., 2011; Arredondo & Billen, 2016; Glerum et al., 2018):

$$\eta_{\text{cp}} = \left( \frac{1}{\eta_{\text{df}}} + \frac{1}{\eta_{\text{ds}}} \right)^{-1} \quad (12)$$

To approximate brittle behavior in our models, a Drucker-Prager plasticity crite-  
 rion is used (e.g., Alejano & Bobet, 2012; Quinquis & Buiter, 2014; Le Pourhiet et al.,  
 2017; Glerum et al., 2018), given by

$$\eta_{\text{p}} = \frac{p \sin \phi + c \cos \phi}{2\dot{\epsilon}_e} \quad (13)$$

where  $c$  is the cohesion and  $\phi$  the angle of friction. The effective viscosity value is then  
 computed assuming that creep mechanisms and plasticity are independent processes (e.g.,  
 Karato, 2008; Andrews & Billen, 2009; Glerum et al., 2018), that is

$$\eta_{\text{eff}} = \min(\eta_{\text{cp}}, \eta_{\text{p}}) \quad (14)$$

195 In order to keep this viscosity within meaningful bounds it is limited to remain in the  
 196 range  $[\eta_{\min}, \eta_{\max}]$ , with typically  $\eta_{\min} = 1 \times 10^{19}$  Pa.s and  $\eta_{\max} = 1 \times 10^{25}$  Pa.s. The ef-  
 197 fective viscosity  $\eta_{\text{eff}}$  is calculated interpolating effective strain rates, pressures and tem-  
 198 peratures of the nodes onto the markers. Elemental viscosities are then calculated as the  
 199 geometric average of  $\eta_{\text{eff}}$  of the markers inside each element.

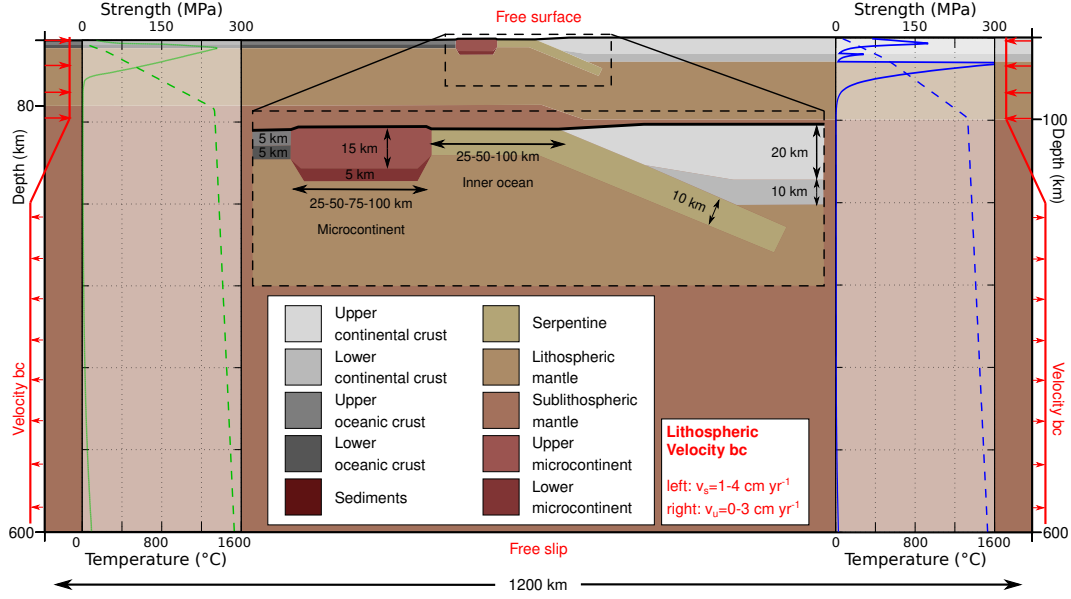


**Figure 1.** Model setup showing crust and mantle lithosphere layer thicknesses with the corresponding temperature (dashed) and strength (continuous) profiles (blue and green for the continental and oceanic domain, respectively). The velocity boundary conditions are in red.

200 Strain softening is taken into account for both plasticity and viscous creep (Huismans  
 201 & Beaumont, 2003; Babeyko & Sobolev, 2005; Huismans et al., 2005; S. V. Sobolev &  
 202 Babeyko, 2005; Warren et al., 2008) by means of the accumulated strain  $\varepsilon_p$  and  $\varepsilon_v$ , re-  
 203 spectively, memorized by each marker. Plastic weakening approximates deformation-induced  
 204 softening of faults and brittle shear zones, while viscous weakening can be interpreted  
 205 as strain-induced grain size reduction and effects of synkinematic metamorphic reactions  
 206 (Warren et al., 2008). Plastic weakening is simulated by a linear decrease with the strain  
 207 of cohesion and angle of friction values, when  $\varepsilon_{p1} < \varepsilon_p < \varepsilon_{p2}$ . Similarly, viscous weak-  
 208 ening linearly reduces the viscosity when the viscous strain  $\varepsilon_v$  is between  $\varepsilon_{v1}$  and  $\varepsilon_{v2}$  (Huismans  
 209 & Beaumont, 2003; Warren et al., 2008).

## 2.2 Numerical setup

211 In this study, we use different setups with various dimensions both of the micro-  
 212 continent and of the inner oceanic domain (Figure 1), in an experimental domain of  $1200 \times$   
 213  $600$  km. The minimum numerical resolution is  $5 \times 5$  km with a horizontal refinement  
 214 towards the center of the model (between  $x = 400$  and  $x = 800$  km) and a vertical  
 215 refinement towards the surface (above 120 km depth) where the maximum resolution is  
 216  $1 \times 1$  km. The total number of elements is 163,200 and each element is initialized with  
 217 16 markers that allow for the tracking of different materials throughout the experiments.  
 218 For time-stepping we use a Courant number of 0.25.

219 The initial thermal structure of the lithosphere corresponds to a simple conduc-  
 220 tive thermal configuration, with a fixed surface temperature of  $0 \text{ }^\circ\text{C}$  and a temperature  
 221 of  $1330 \text{ }^\circ\text{C}$  at its base (e.g., Erdős et al., 2019; Marotta et al., 2020; Regorda et al., 2021,  
 222 2023). The temperature of the sublithospheric mantle follows an adiabatic gradient of  
 223  $0.4 \text{ }^\circ\text{C km}^{-1}$  that leads to a temperature of  $1530 \text{ }^\circ\text{C}$  at 600 km depth (e.g., Salazar-Mora  
 224 et al., 2018; Theunissen & Huismans, 2019). No heat flow is allowed across the side bound-  
 225 aries. All the rheological and thermal parameters can be found in Table 1.

**Table 1.** Densities and plastic, viscous, and thermal parameters of the materials used in the models. Crustal and lithospheric thicknesses in brackets refer to the microcontinents. The variation of the sublithospheric thicknesses refer to domains below continental and oceanic lithospheric mantle, respectively.

Parameter	Symbol	Units	Continental Crust		Oceanic Crust		Sediments	Serpentine	Mantle	
			Upper	Lower	Upper	Lower			Lithospheric	Sublithospheric
Thickness	-	km	20 (15)	10 (5)	5	5	-	-	70 (60)	500-520
Density <sup>a,b,c,d</sup>	$\rho$	kg m <sup>-3</sup>	2750	2900	3200		2650	3000	3300	
Plastic weakening range <sup>e</sup>	$\varepsilon_{p1}-\varepsilon_{p2}$	-	0.5-1.5		0.5-1.5		0.5-1.5	0.5-1.5	0.5-1.5	
Friction angle <sup>f</sup>	$\phi$	°	25-5		15-3	25-5	25-5	25-5	25-5	
Cohesion <sup>e,f</sup>	$c$	MPa	20-4		10-2	20-4	20-4	20-4	20-4	
Viscous weakening range <sup>f</sup>	$\varepsilon_{v1}-\varepsilon_{v2}$	-	1-5		1-5		1-5	1-5	1-5	
Viscous weakening factor <sup>f</sup>	$f_{vw}$	-	10		10		10	10	10	
Flow law*			Dry granite <sup>g</sup>	Felsic granulite <sup>h</sup>	Antigorite <sup>a</sup>	Microgabbro <sup>h,i</sup>	Wet granite <sup>g</sup>	Antigorite <sup>a</sup>	Dry olivine <sup>l</sup>	
<i>Dislocation creep</i>										
Pre-exponential factor	$A_{ds}$	(Pa s <sup>-1</sup> )	$1.14 \times 10^{-28}$	$2 \times 10^{-21}$	$1.39 \times 10^{-37}$	$1.99 \times 10^{-11}$	$7.96 \times 10^{-16}$	$1.39 \times 10^{-37}$	$1.1 \times 10^{-16}$	
Stress exponent	$n_{ds}$	-	3.2	3.1	3.8	3.4	1.9	3.8	3.5	
Activation energy	$Q_{ds}$	(kJ mol <sup>-1</sup> )	123	243	89	497	140	89	530	
Activation volume	$V_{ds}$	(m <sup>3</sup> mol <sup>-1</sup> )	0		$0.32 \times 10^{-5}$	0	0	$0.32 \times 10^{-5}$	$1.8 \times 10^{-5}$	
<i>Diffusion creep</i>										
Pre-exponential factor	$A_{df}$	(Pa s <sup>-1</sup> )	-		-	-	-	-	$2.37 \times 10^{-15}$	
Activation energy	$Q_{df}$	(kJ mol <sup>-1</sup> )	-		-	-	-	-	375	
Activation volume	$V_{df}$	(m <sup>3</sup> mol <sup>-1</sup> )	-		-	-	-	-	$1 \times 10^{-5}$	
Grain size	$d$	(mm)	-		-	-	-	-	5	
Grain size exponent	$m$	-	-		-	-	-	-	3	
<i>Thermal parameters</i>										
Heat capacity <sup>a,f,m</sup>	$C_p$	(m <sup>2</sup> K s <sup>-2</sup> )	800		800		800	1250	1250	
Conductivity <sup>a,d</sup>	$k$	(W m <sup>-1</sup> K <sup>-1</sup> )	3.2	2.1	1.8	2.6	3.2	2.25	2.25	
Thermal expansion <sup>a,f</sup>	$\alpha$	(K <sup>-1</sup> )	$3.28 \times 10^{-5}$		$3.28 \times 10^{-5}$		$3.28 \times 10^{-5}$	$3 \times 10^{-5}$	$3 \times 10^{-5}$	
Heat production <sup>d,e</sup>	$H$	( $\mu$ W m <sup>-2</sup> )	1.3		0.2		1.3	0	0	

\* The Stokes solver tolerance and the maximum number of iterations have been fixed to  $10^{-3}$  and 100, respectively.

References: <sup>a</sup>Petersen and Schiffer (2016); <sup>b</sup>Gerya et al. (2004); <sup>c</sup>Gerya and Yuen (2003); <sup>d</sup>Naliboff and Buitert; <sup>e</sup>Naliboff et al. (2020); <sup>f</sup>Warren et al. (2008); <sup>g</sup>Ranalli (1995);

<sup>h</sup>Wilks and Carter (1990); <sup>i</sup>Burov (2011); <sup>l</sup>Hirth and Kohlstedt (2003); <sup>m</sup>Rolf et al. (2018).

226 We consider a 20 km thick upper continental crust with a 10 km thick lower con-  
 227 tinental crust for the upper plate, and a 5 km thick upper oceanic and a 5 km thick lower  
 228 oceanic crust for the subducting plate. We also consider a 70 km thick lithospheric man-  
 229 tle for both plates, resulting in a 100 km thick lithosphere for the upper plate and in a  
 230 80 km thick lithosphere for the subducting plate. The microcontinents are placed on the  
 231 subducting plate and they are characterized by a 15 km thick upper crust and a 5 km  
 232 thick lower crust on top of a 60 km thick lithospheric mantle (Table 1 and Figure 1). In  
 233 order to initiate the subduction, we use a weak seed between the upper and lower plate,  
 234 consisting of a 10 km thick serpentine layer up to 50 km depth, that will eventually evolve  
 235 into a subduction channel (e.g., De Franco et al., 2008a; Tetreault & Butier, 2012). The  
 236 initial topography is given by the isostatic re-equilibration of the system.

237 Here, we tested microcontinents of various dimensions (25, 50, 75, and 100 km) placed  
 238 at different distances from the continental plate (inner ocean size: 25, 50, and 100 km).  
 239 We also examined different inflow velocities set along both vertical boundaries. We set  
 240 inflow velocities from the surface down to the bottom of the lithosphere at 1 and 4  $\text{cm yr}^{-1}$   
 241 on the left side of the domain (subducting oceanic plate) and 0 and 3  $\text{cm yr}^{-1}$  on the right  
 242 side (upper continental plate). The velocities on the oceanic plate were chosen to sim-  
 243 ulate slow and intermediate subductions. A velocity of 3  $\text{cm yr}^{-1}$  on the continental plate  
 244 was selected to analyze the effects of the upper plate movement, considering velocities  
 245 higher or lower than the subducting plate. Moreover, these velocities allow us to inves-  
 246 tigate whether the geodynamics of the subductive system is affected solely by the total  
 247 convergent velocity or the distribution of velocities among the plates also influences the  
 248 thermo-mechanics of the system. In all models, a constant outflow velocity along the ver-  
 249 tical boundaries in the asthenosphere and a linear transitional zone of 100 km were set,  
 250 ensuring that the net material flux along the vertical boundaries is 0. The models evolved  
 251 for different times required to achieve a final convergence of 300 km. All the simulations  
 252 tested are summarized in Table 2.

### 253 3 Results

254 Throughout this work, the models are identified by their unique model identifier,  
 255 as shown in the first column of Table 2 that provides information about the dimension  
 256 of the microcontinent (MC), followed by indicators of the dimension of the inner ocean  
 257 (IO) between the microcontinent and the upper plate, and the velocities of both the sub-  
 258 ducting ( $vs$ ) and the upper ( $vu$ ) plates. For example, the identifier  $S9_{25}.IO_{100}.vs_1.vu_0$   
 259 is used for a model with a small (S9) microcontinent (25 km), an inner ocean of 100 km  
 260 ( $IO_{100}$ ), a subducting plate velocity ( $vs$ ) of 1  $\text{cm yr}^{-1}$ , and an upper plate velocity ( $vu$ )  
 261 of 0  $\text{cm yr}^{-1}$ . In case of models without microcontinent (models NM), the model iden-  
 262 tifier is only followed by the the plates velocities.

263 Firstly, we present the results of models without a microcontinent (models NM in  
 264 Table 2) to verify whether different velocities of both plates affect the thermo-mechanical  
 265 evolution of the subduction system. Subsequently, we present the modeling results for:  
 266 1) models with small microcontinents (25 km; models S in Table 2); 2) models with medium  
 267 microcontinents (50 km; models M in Table 2); 3) models with large microcontinents (75  
 268 km; models L in Table 2); and 4) models with extra-large microcontinents (100 km; mod-  
 269 els XL in Table 2).

270 For all these models, we first discuss the cases with a narrow inner ocean (25 km-  
 271 wide), comparing their thermo-mechanical evolution with models without microconti-  
 272 nents characterized by the same velocities (models NM in Table 2). After that, we an-  
 273 alyze the thermo-mechanical impact of different dimensions of the inner ocean (50 and  
 274 100 km). The effects on the thermal state are analyzed through three geotherms located  
 275 at 50, 75, and 100 km from the trench, identified as  $\text{geotherm}_{50}$ ,  $\text{geotherm}_{75}$ , and  $\text{geotherm}_{100}$ ,  
 276 respectively. All geotherms have been calculated exclusively above the slab to highlight

**Table 2.** Setup for the different models tested. The following parameters have been varied: dimension of the microcontinent (MC); dimension of the inner ocean (IO) located between the microcontinent and the upper plate; upper plate (UP) velocity; subducting plate (SP) velocity; duration of the evolution (model time). The models are shown in the figures listed in the last column.

Model	MC dimension (km)	IO dimension (km)	SP velocity (cm yr <sup>-1</sup> )	UP velocity (cm yr <sup>-1</sup> )	Model time (Myr)	Figures
NM1	1	0	-	-	30	Figure 2a, e and i
NM2	1	3	-	-	7.5	Figure 2b, f and l
NM3	4	0	-	-	7.5	Figure 2c, g and m
NM4	4	3	-	-	4.5	Figure 2d, h and n
S1	25	25	1	0	30	Figure 3a and e
S2	25	25	1	3	7.5	Figure 3b and f
S3	25	25	4	0	7.5	Figure 3c and g
S4	25	25	4	3	4.5	Figure 3d and h
S5	25	50	1	0	30	Figure 5a and d
S6	25	50	1	3	7.5	-
S7	25	50	4	0	7.5	-
S8	25	50	4	3	4.5	-
S9	25	100	1	0	30	Figure 5b and e
S10	25	100	1	3	7.5	-
S11	25	100	4	0	7.5	Figure 5c and f
S12	25	100	4	3	4.5	-
M1	50	25	1	0	30	Figure 6a, e and i
M2	50	25	1	3	7.5	Figure 6b, f and l
M3	50	25	4	0	7.5	Figure 6c, g and m
M4	50	25	4	3	4.5	Figure 6d, h and n
M5	50	50	1	0	30	-
M6	50	50	1	3	7.5	Figure 8a, e and i
M7	50	50	4	0	7.5	-
M8	50	50	4	3	4.5	-
M9	50	100	1	0	30	Figure 8b, f and l
M10	50	100	1	3	7.5	Figure 8c, g and m
M11	50	100	4	0	7.5	Figure 8d, h and n
M12	50	100	4	3	4.5	-
L1	75	25	1	0	30	-
L2	75	25	1	3	7.5	-
L3	75	25	4	0	7.5	Figure 9a, c and e
L4	75	25	4	3	4.5	Figure 9b, d and f
L5	75	50	1	0	30	-
L6	75	50	1	3	7.5	-
L7	75	50	4	0	7.5	Figure 11a, d and g
L8	75	50	4	3	4.5	-
L9	75	100	1	0	30	-
L10	75	100	1	3	7.5	-
L11	75	100	4	0	7.5	Figure 11b, e and h
L12	75	100	4	3	4.5	Figure 11c, f and i
XL1	100	25	1	0	30	Figure 12a, e and i
XL2	100	25	1	3	7.5	-
XL3	100	25	4	0	7.5	-
XL4	100	25	4	3	4.5	-
XL5	100	50	1	0	30	-
XL6	100	50	1	3	7.5	-
XL7	100	50	4	0	7.5	Figure 12b, f and l
XL8	100	50	4	3	4.5	-
XL9	100	100	1	0	30	-
XL10	100	100	1	3	7.5	-
XL11	100	100	4	0	7.5	Figure 12c, g and m
XL12	100	100	4	3	4.5	Figure 12d, h and n

277 differences in the thermal state of the mantle wedge, which are crucial for understand-  
 278 ing the metamorphic evolution of subducted and exhumed crustal rocks. These geotherms  
 279 are presented from the surface to 25, 45, and 80 km depth for geotherm<sub>50</sub>, geotherm<sub>75</sub>,  
 280 and geotherm<sub>100</sub>, respectively.

### 281 **3.1 Models without microcontinent - models NM**

#### 282 **3.1.1 Model with $v_s=1$ cm yr<sup>-1</sup> and $v_u=0$ cm yr<sup>-1</sup> - model NM1**

283 The reference model NM1, characterized by a slow subducting plate velocity ( $v_s=1$   
 284 cm yr<sup>-1</sup>) and a fixed upper plate velocity ( $v_u=0$  cm yr<sup>-1</sup>), exhibits the classical evolu-  
 285 tion of subduction systems. It shows the development of a subduction channel charac-  
 286 terized by high strain rates (exceeding  $10^{-14}$  s<sup>-1</sup>), which facilitates the initiation of sub-  
 287 duction (blue-to-white area in Fig. 2a and Movie S1 in the Supporting Information).

288 During the initial phase, the coupling between the two plates results in elevated  
 289 topography in the forearc region and a slight advancement of the trench (approximately  
 290 30 km; indicated by the red star in Fig. 2i). This phase concludes when a continuous  
 291 subduction channel forms up to the bottom of the lithosphere. However, the coupling  
 292 is not strong enough to induce ablation of continental crust from the upper plate, result-  
 293 ing in no recycling of continental crust in the wedge.

294 Subsequently, the trench experiences slow retreat (approximately 30 km) due to  
 295 the collapse of the topography developed in the forearc, leading to the advancement of  
 296 the accretionary wedge toward the subducting plate (indicated by the green star in Fig.  
 297 2i). During the second half of the evolution, as the subduction channel becomes well-  
 298 formed and continuous (Fig. 2e and Movie S1 in the Supplementary Information), all  
 299 forces balance out, and both the trench and the topography show no further variation  
 300 (Fig. 2i).

#### 301 **3.1.2 Effects of plates velocities - models NM2-NM4**

302 The imposition of a velocity on the upper plate (model *NM2.v<sub>s1</sub>.v<sub>u3</sub>*) results in  
 303 higher coupling between the plates, leading to the development of a higher strain rate  
 304 in the forearc region during the initial phase of the evolution (Fig. 2b). However, due  
 305 to the higher value of  $v_u$  compared to  $v_s$  ( $v_s=1$  cm yr<sup>-1</sup> and  $v_u=3$  cm yr<sup>-1</sup>), this model  
 306 does not exhibit any advancement of the trench, which consistently retreats for the en-  
 307 tire duration of the simulation (approximately 200 km; Fig. 2l), in contrast to the be-  
 308 havior observed in model NM1. On the contrary, the evolution of the topography is char-  
 309 acterized by a continuous decrease in the maximum height after the development of a  
 310 continuous subduction channel (Fig. 2l), as observed in model NM1. The continuous ad-  
 311 vancement of the upper plate results in a decrease in the dip angle of the shallowest por-  
 312 tion of the slab (above 50 km), which is 24° (Fig. 2f), compared to 28° calculated in the  
 313 model with the fixed upper plate (model NM1; Fig. 2e). Nevertheless, the final dynam-  
 314 ics are similar to that observed in model NM1, with no ablation of continental crust from  
 315 the upper plate.

316 Model *NM3.v<sub>s4</sub>.v<sub>u0</sub>* is characterized, like model NM2, by a total convergent ve-  
 317 locity of 4 cm yr<sup>-1</sup> ( $v_s=4$  cm yr<sup>-1</sup> and  $v_u=0$  cm yr<sup>-1</sup>). However, the coupling between  
 318 the plates and the general dynamics are remarkable different from the previous model.  
 319 Model NM3 shows the development of bands with high strain rates that cross the en-  
 320 tire thickness of the continental crust of the upper plate during the initial phase of the  
 321 evolution (Fig. 2c and Movie S2 in the Supplementary Information), as a result of higher  
 322 coupling compared to models NM1 and NM2 (Fig. 2a and b, respectively). Consequently,  
 323 the maximum topography developed is higher, and there is an initial advancement of the  
 324 trench of approximately 100 km, marked by a red star in Fig. 2m. The higher coupling  
 325 also results in the ablation of upper and lower continental crust from the upper plate,

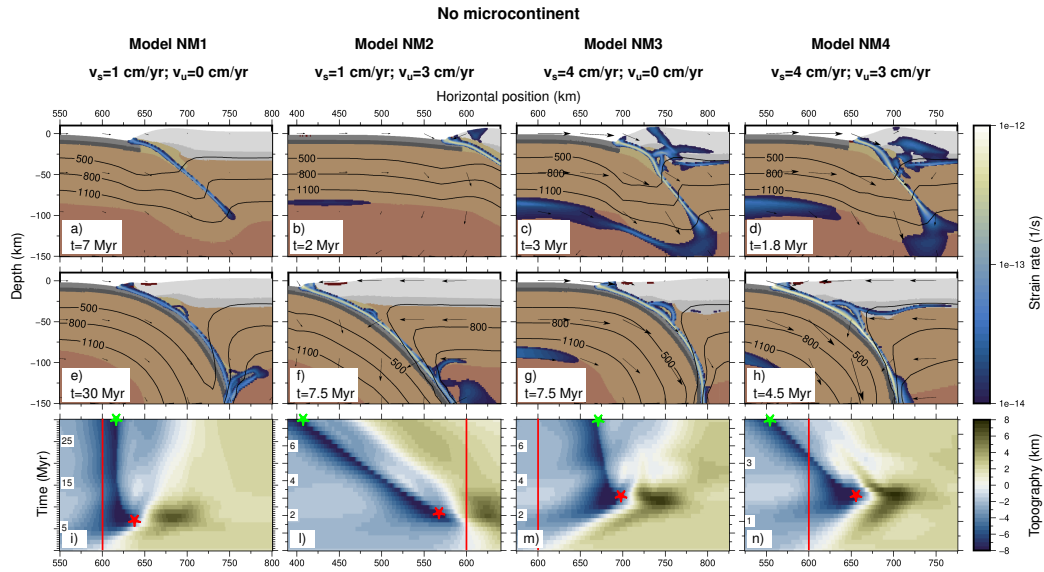


**Figure 2.** The evolution of models without a microcontinent at two distinct stages, including velocity fields and strain rates (panels a-h), and the evolution of topography throughout the entire duration of simulations (panels i-n) are presented for different velocities of the subducting plate ( $v_s$ ) and the upper plate ( $v_u$ ). Black lines on the figures indicate 500, 800, and 1100 °C isotherms, while background colors define the composition as in Fig. 1. Red lines indicate the initial position of the trench, and red stars represent the trench position at the time shown in the first row, indicating the maximum advancement. Green stars indicate the maximum retreat of the trench.

326 leading to slight recycling in the wedge during the second half of the evolution (Fig. 2g),  
 327 unlike models NM1 and NM2. However, the second part of the simulation is similar to  
 328 what was observed for the previous models, with a continuous collapse of the topogra-  
 329 phy of the upper plate that leads to a slight retreat of the trench (approximately 30 km;  
 330 Fig. 2m). The final geometry of the slab is also similar to that of the reference model  
 331 (NM1), with a shallow dip angle of the slab of 28° (Fig. 2g)

332 Model *NM4.v<sub>s4</sub>.v<sub>u3</sub>* ( $v_s=4$  cm yr<sup>-1</sup> and  $v_u=3$  cm yr<sup>-1</sup>) exhibits characteristics found  
 333 both in model NM2 and in models NM1 and NM3. In fact, high velocities imposed on  
 334 both plates result in high strain rates in the upper plate (Fig. 2d) and, consequently, high  
 335 topography (Fig. 2n), similar to the pattern observed in model NM3 (Fig. 2m). Sim-  
 336 ilarly, the higher velocity of the subducting plate leads to an initial advancement of the  
 337 trench (approximately 60 km) in the initial 2 Myr of evolution (red star in Fig. 2n), re-  
 338 sembling the behavior of models NM1 and NM3 (red stars in Fig. 2i and m). However,  
 339 the imposed velocity on the upper plate limits this advancement, which is less than in  
 340 model NM3, and results in a pronounced trench retreat in the second half of the simu-  
 341 lation (approximately 100 km; green star in Fig. 2n), akin to the behavior observed in  
 342 model NM2 characterized by low  $v_s$  and high  $v_u$  (Fig. 2l). This is related, as in the pre-  
 343 vious models, to the development of a continuous subduction channel (Fig. 2h) that leads  
 344 to a decrease in strain rates in the upper plate and the consequent collapse of the topog-  
 345 raphy (Fig. 2n). Lastly, the velocity imposed on the upper plate causes a decrease in the  
 346 shallow slab dip, albeit to a limited extent due to the high velocity of the subducting plate.  
 347 The final dip angle is 26°, between the angles calculated for models NM1 and NM3 (28°)  
 348 and for model NM2 (24°).

## 349 **3.2 Models with 25 km-wide microcontinent - models S**

### 350 **3.2.1 Models with 25 km-wide inner ocean - models S1-S4**

351 In cases involving models with small microcontinents (25 km-wide) and a narrow  
 352 inner ocean (25 km-wide; models S1-S4 in Fig. 3), the microcontinents do not accrete  
 353 at the trench. Consequently, the accretionary wedge is primarily composed of sediments,  
 354 resembling the models without microcontinents (refer to models NM1-NM4 in Fig. 2).  
 355 As a result, a significant amount of continental material is subducted and subsequently  
 356 exhumed in the mantle wedge (Fig. 3a-d). Differences emerge in the ability to recycle  
 357 and eventually exhume subducted material, influenced by variations in the velocities of  
 358 the subducting and upper plates.

359 In particular, for  $v_s = 1$  cm yr<sup>-1</sup> and a fixed upper plate (model *S1<sub>25</sub>.IO<sub>25</sub>.v<sub>s1</sub>.v<sub>u0</sub>*),  
 360 there is exhumation of almost the entire microcontinent, rising from a maximum depth  
 361 of approximately 140 km to 10-15 km depth (Fig. 3a and Movie S3 in the Supporting  
 362 Information). This exhumation occurs due to a detachment between upper and lower  
 363 crust of the microcontinent when it is already subducted (at approximately 40 km depth),  
 364 facilitating detachment from the slab and subsequent recycling. The exhumation of a  
 365 significant amount of continental material promotes the upwelling of subducted oceanic  
 366 material and has a slight effect on the shallow slab dip angle, decreasing from 28° in model  
 367 NM1 to 25°. During the first half of evolution, the subduction of the microcontinent does  
 368 not affect neither the trench advancement nor the topography with respect to model NM1  
 369 (Fig. 3e). However, model S1 exhibits an additional retreat of the trench during the last  
 370 7 million years of evolution (yellow star in Fig. 3e), attributed to the upwelling of ma-  
 371 terial pushing the accretionary wedge toward the subducting plate (Fig. 3a and Movie  
 372 S3 in the Supporting Information). As a consequence, the topography in the upper plate  
 373 undergoes changes, marked by the formation of a pronounced basin on the forearc.

374 The upwelling flow to shallow depths, resulting from the exhumation of continen-  
 375 tal material in the internal portion of the mantle wedge (profiles  $p_1$  and  $p_2$  in Fig. 3a),  
 376 together with higher radiogenic heating, induces a temperature increase of approximately

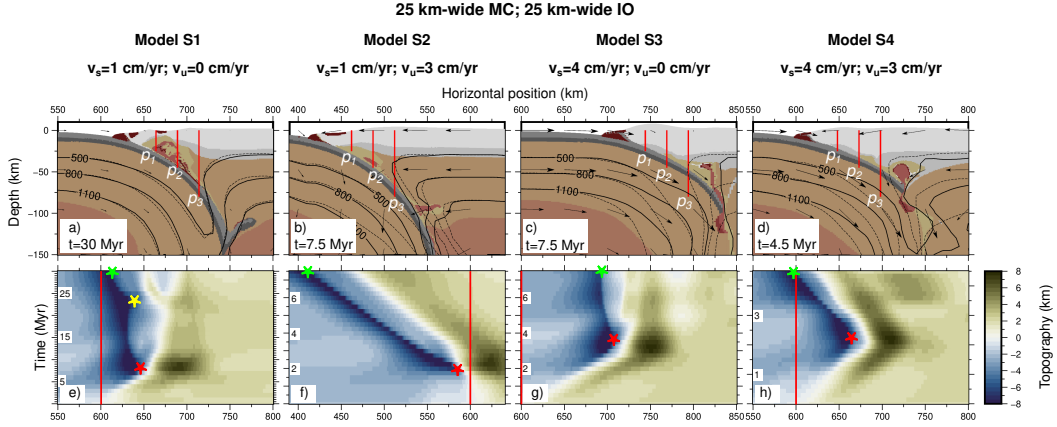


**Figure 3.** The evolution of models with a 25 km-wide microcontinent (MC) and a 25 km-wide inner ocean (IO), including velocity fields and strain rates (panels a-d), and the evolution of topography throughout the entire duration of simulations (panels e-h) are presented for different velocities of the subducting plate ( $v_s$ ) and the upper plate ( $v_u$ ). Red lines on panels a-d ( $p_1$ ,  $p_2$  and  $p_3$ ) indicate the position of the thermal profiles shown in Fig. 4. Black lines indicate 500, 800 and 1100 °C isotherms, while dashed black lines indicate the same isotherms referred to NM1 model. Background colors define the composition as in Fig. 1. In panels e-h, red lines and red stars indicate the initial position and the maximum advancement of the trench, respectively, while the green stars indicate the maximum retreat of the trench. Yellow star indicates the beginning of exhumation of subducted material.

377 50 °C in the mantle wedge up to 75 km from the trench (continuous light blue lines in  
 378 Fig. 4a and b), compared to the model without the microcontinent (model NM1; con-  
 379 tinuous black lines in Fig. 4a and b). In contrast, the dynamics in the mantle wedge at  
 380 100 km from the trench is not affected by the exhumation of continental material (pro-  
 381 file  $p_3$  in Fig. 3a), resulting in no difference in the thermal state compared to model NM1  
 382 (see continuous light blue and black lines in Fig. 4c).

383 Conversely, a velocity on the upper plate higher than that on the subducting plate  
 384 (model  $S2_{25}.IO_{25}.vs_1.vu_3$ ;  $v_s = 1$  and  $v_u = 3$  cm yr $^{-1}$ ) induces a more vigorous man-  
 385 tle flux in the mantle wedge compared to the preceding model (model S1), which lim-  
 386 its the recycling of subducted material (Fig. 3b). As the exhumation of material is lim-  
 387 ited, it has no effects on the topography (Fig. 3f) compared to the topography evolu-  
 388 tion observed for model NM2 (Fig. 2l). Similarly, the slab dip angle above 50 km depth  
 389 remains the same as in the model without the microcontinent (24°). However, there is  
 390 a clear increase in the dip angle below 50 km depth, which is easily recognizable when  
 391 comparing the isotherms in Fig. 3b.

392 The thermal state in the internal portion of the mantle wedge (profiles  $p_1$  and  $p_2$   
 393 in Fig. 3b) is only slightly higher than in model NM2 (less than 50 °C). This modest in-  
 394 crease is due to the limited amount of recycled material, evident in the geotherm50 and  
 395 geotherm75 at depths below 35-40 km. As observed in model S1, the thermal state in  
 396 the external portion of the wedge (profile  $p_3$  in Fig. 3b) is the same as in model NM2.

397 The evolution of models with  $v_s = 4$  cm yr $^{-1}$  (models  $S3_{25}.IO_{25}.vs_4.vu_0$  and  $S4_{25}.IO_{25}.vs_4.vu_3$ )  
 398 is very similar and is not influenced by the velocity of the upper plate. Both models ex-  
 399 hibit the exhumation of continental crust, originating from both the microcontinent and  
 400 ablated from the upper plate (Fig. 3c and d). This is attributed to the higher coupling

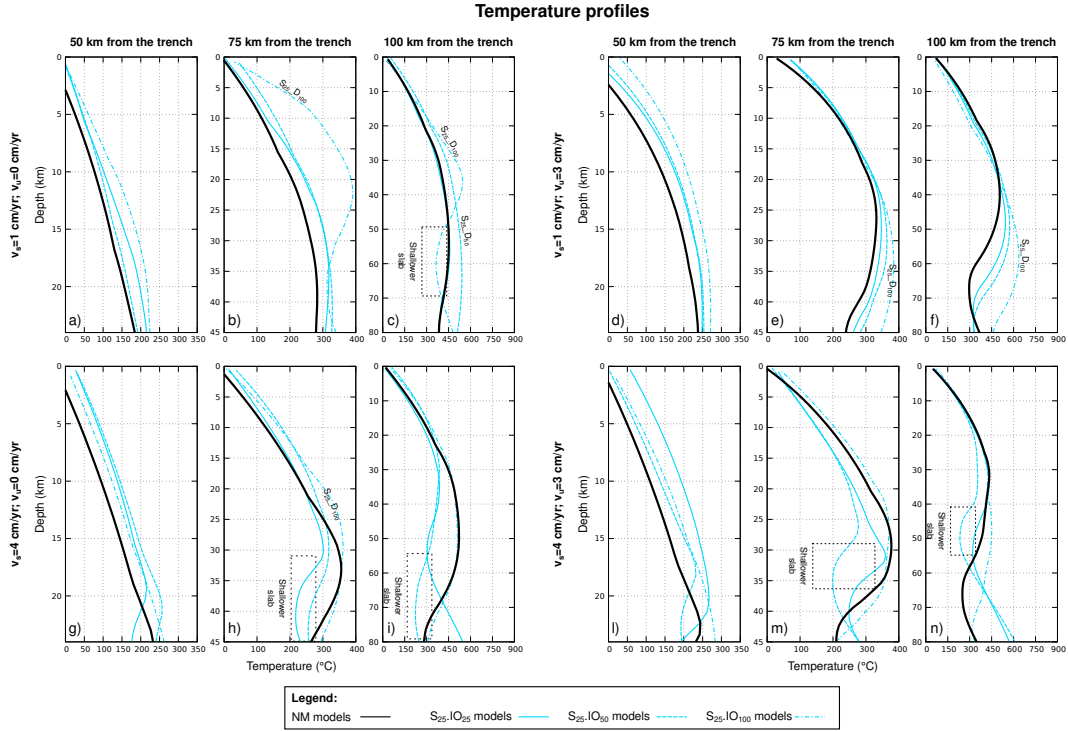


**Figure 4.** Temperature profiles for models with 25 km-wide microcontinent at different distances from the trench: 50 km (panels a, d, g, and l), 75 km (panels b, e, h, and m), and 100 km (panels c, f, i and, n). Continuous black lines indicate the profiles of models without microcontinents (NM). Continuous cyan lines indicate models with 25 km-wide inner ocean, dashed lines indicate models with 50 km-wide inner ocean, and dashed-dotted lines indicate models with 100 km-wide inner ocean.

401 between the plates, as previously observed in models NM3 and NM4. However, the  
 402 recycling of material in these models occurs farther from the trench than in model S1 and  
 403 beneath a thicker crust. This allows exhumation from a depth of 80 km up to approx-  
 404 imately 40 km but not shallower (Fig. 3c and d). Consequently, the evolution of the to-  
 405 pography is also similar to that observed in models without a microcontinent (models  
 406 NM3 and NM4), because of the slight effects of the exhumed material (Fig. 3g and h).

407 The recycling of subducted material in the external portion of the mantle wedge  
 408 weakens the mantle flux, as evidenced by the isotherm at 500 °C, which is farther from  
 409 the trench in the wedge area compared to models NM3 and NM4 (compare continuous  
 410 and dashed isotherms in Fig. 3c and d). The diminished mantle flux results in a less steep  
 411 slab, with a decrease in the slab dip angle from 28° to 22° for models with a fixed up-  
 412 per plate (models NM3 and S3, respectively) and from 26° to 21° for models with  $v_u =$   
 413  $3 \text{ cm yr}^{-1}$  (models NM4 and S4, respectively; observe differences between continuous and  
 414 dashed isotherms in Fig. 3c and d). As a consequence, the temperature in the mantle  
 415 wedge at 75 and 100 km from the trench decreases compared to NM models (continu-  
 416 ous light blue lines in Fig. 4h, i, m, and n). In contrast, there is an increase of 50-100  
 417 °C in the temperatures in the most internal portion of the wedge (continuous light blue  
 418 lines in Fig. 4g and l), as observed in the previous models.

### 419 **3.2.2 Effects of wider inner oceans - models S5-S12**

420 The increase in the dimension of the inner ocean (50 and 100 km, models S5-S12)  
 421 does not significantly impact the thermo-mechanical evolution of the models. In the first  
 422 half of the simulation, the topography evolution follows a pattern similar to that of the  
 423 previous models, featuring an initial advancement (red stars in Fig. 5d and e) followed  
 424 by a lesser retreat. On the contrary, a larger inner ocean generates a well-developed and  
 425 lubricated subduction channel that facilitates the subduction of the microcontinent. Model  
 426  $S5_{25}.IO_{50}.vs_1.vu_0$  is characterized by a steeper slab dip compared to models NM1 and  
 427 S1, resulting in a warmer geotherm within the mantle wedge (Fig. 4a, b, c).

428 In model  $S9_{25}.IO_{100}.vs_1.vu_0$ , the microcontinent's initial location, farther from the  
 429 upper plate, ensures that when it collides, the subduction channel is already fully de-  
 430 veloped. Consequently, its collision leads to a slight advancement of the trench after ap-  
 431 proximately 15 million years of evolution (pink star in Fig. 5e), not observed in previ-  
 432 ous models. Afterward, the trench remains stable for a few million years, until the ex-  
 433 humation of a substantial amount of subducted material causes an advancement of the  
 434 accretionary wedge toward the subducting plate, resulting in a subsequent retreat of the  
 435 trench (yellow star in Fig. 5e). Unlike other models, the S9 model still allows for easy  
 436 subduction of the microcontinent, but the presence of a large amount of serpentized  
 437 crust related to a 100 km-wide inner ocean induces the exhumation of abundant subducted  
 438 material from approximately 140 km depth up to the surface (Fig. 5b and Movie S4 in  
 439 the Supporting Information). As a consequence, a more gentle slab dip occurs compared  
 440 to models NM1, decreasing from 28° to 21° (dashed and continuous black lines, respec-  
 441 tively, in Fig. 5b), and there is an increase in temperature by up to 150-200 °C in the  
 442 central part of the mantle wedge compared to model S1. This difference is clearly vis-  
 443 ible when comparing geotherm75 and geotherm100 (dotted-dashed light blue lines in Fig.  
 444 4b and c).

445 A 100 km-wide inner ocean does not have any effect on models  $S10_{25}.IO_{100}.vs_1.vu_3$   
 446 and  $S12_{25}.IO_{100}.vs_4.vu_3$ , while a few differences can be observed in model  $S11_{25}.IO_{100}.vs_4.vu_0$ .  
 447 Specifically, unlike model S3, which showed a temperature decrease in the mantle wedge,  
 448 model S11 is characterized by an increase in temperature of approximately 50 °C com-  
 449 pared to the model without the microcontinent (dashed-dotted light blue and continu-  
 450 ous black lines in Fig. 4h). In fact, unlike model S3, this model exhibits a slab dip an-

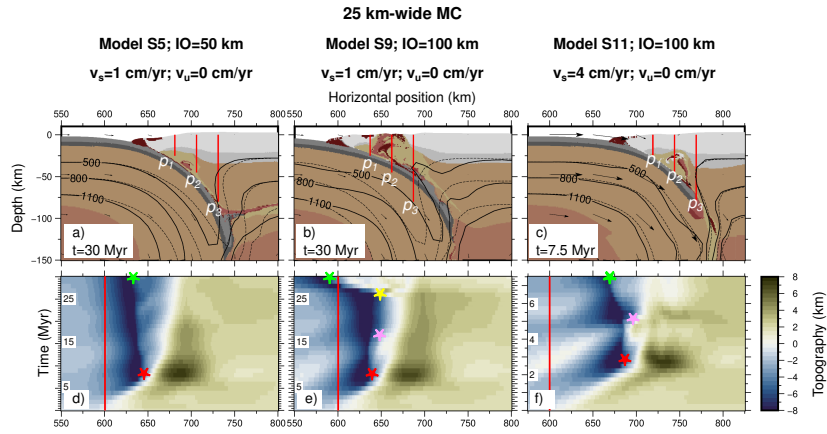


**Figure 5.** The evolution of models with a 25 km-wide microcontinent (MC) and 50 (panel a) and 100 (panels b and c) km-wide inner ocean (IO), including velocity fields, and the evolution of topography throughout the entire duration of simulations (panels d-f) are presented for different velocities of the subducting plate ( $v_s$ ) and the upper plate ( $v_u$ ). Red lines on panels a-c ( $p_1$ ,  $p_2$ , and  $p_3$ ) indicate the position of the thermal profiles shown in Fig. 4. Black lines indicate 500, 800 and 1100 °C isotherms, while dashed black lines indicate the same isotherms referred to NM models. Background colors define the composition as in Fig. 1. In panels d-f, red lines and red stars indicate the initial position and the maximum advancement of the trench, respectively, while the green stars indicate the maximum retreat of the trench. Pink stars indicate the collision of the microcontinent and yellow star indicates the beginning of exhumation of subducted material.

451 gle similar to model NM3 (see isotherm in Fig. 5c), and in this case, the recycling of con-  
 452 tinental material in the mantle wedge can contribute to a temperature increase.

453 On the contrary, the upwelling of subducted crust is not intense enough to provoke  
 454 a trench retreat, as observed in models S1 and S9. The final retreat (green star in Fig.  
 455 5f) is due to the collapse of the topography of the upper plate, similar to model NM3.  
 456 Nonetheless, the total retreat is less than in models NM3 because the collision and sub-  
 457 sequent subduction of the microcontinent result in a temporary advancement of the trench  
 458 after 5 million years (pink star in Fig. 5f).

### 459 **3.3 Models with 50 km-wide microcontinent - models M**

#### 460 **3.3.1 Models with 25 km-wide inner ocean - models M1-M4**

461 The introduction of a larger microcontinent (MC=50 km) in the case of a small in-  
 462 ner ocean (IO=25 km; models M1-M4) induces high coupling between the plates when  
 463 the microcontinent collides. In models with a low velocity of the subducting plate ( $M1_{50}.IO_{25}.vs_1.vu_0$   
 464 and  $M2_{50}.IO_{25}.vs_1.vu_3$ ), this results in the accretion of the microcontinent at the trench,  
 465 a jump of subduction backward (from  $s_1$  to  $s_2$  in Fig. 6a and b and Movies S5 in the  
 466 Supporting Information), and subsequent detachment between the upper and lower con-  
 467 tinental crust, the latter being subducted. A forced trench retreat is thus observed (just  
 468 after the red stars in Fig. 6i and l). However, the development of the new subduction  
 469 channel ( $s_2$  in Fig. 6a and b) occurs while the original channel is still active ( $s_1$  in Fig.  
 470 6a and b), and, therefore, subduction is continuous throughout the entire evolution of  
 471 these models.

472 Differently, the higher coupling observed in models with high velocities of the sub-  
 473 ducting plate (models M3 and M4) results in a temporary interruption of the subduc-  
 474 tion (approximately 0.5 Myr) after the collision of the microcontinent (models  $M3_{50}.IO_{25}.vs_4.vu_0$   
 475 and  $M4_{50}.IO_{25}.vs_4.vu_3$  in Fig. 6c and d). As a consequence, the strain rates in the shal-  
 476 lowest part of the subduction channel decrease, and a back thrust fault develops behind  
 477 the accretionary wedge ( $b_1$  in Fig. 6c and d and Movie S6 in the Supporting Informa-  
 478 tion). After that, the subduction restarts along a new subduction channel backward of  
 479 the microcontinent ( $s_2$  in Fig. 6c and d), with the detachment of the lower crust of the  
 480 microcontinent and its subsequent subduction (Fig. 6g and h and Movie S7 in the Sup-  
 481 porting Information). Since models M1, M2, M3 and M4 are characterized by the sub-  
 482 duction of a small part of the microcontinent (primarily the lower crust), the recycling  
 483 of subducted material in the mantle wedge is very limited (Fig. 6e-h).

484 From a thermal point of view, models M2, M3 and M4 are characterized by both  
 485 a slight warming of approximately 25-50 °C in the most internal portion of the wedge  
 486 (red continuous lines in Fig. 7d, l, and g) and a cooling of up to 100-150 °C along more  
 487 external profiles (red continuous lines in Fig. 7e, f, h, i, n, and m) compared to the mod-  
 488 els without a microcontinent. The slight warming is attributed to the limited amount  
 489 of crustal material recycled in the mantle wedge. On the contrary, the significant cool-  
 490 ing in the external part of the mantle wedge is attributed to the shallow slab (slab dip  
 491 of 21°) resulting from the collision of the microcontinent and the restart of subduction  
 492 backward (Fig. 6g, h). On the contrary, model M1 shows no differences compared to model  
 493 NM1 because the low velocities imposed at the boundaries result in a low global man-  
 494 tle flow. Therefore, the presence of limited amount of continental material has only a  
 495 slight effect on the mantle flow inside the wedge (see isotherms in Fig. 6e).

#### 496 **3.3.2 Effects of wider inner oceans - models M5-M12**

497 The increase in the dimension of the inner ocean to 50 km does not significantly  
 498 affect the subduction dynamics compared to the models with a smaller inner ocean, ex-  
 499 cept for model  $M6_{50}.IO_{50}.vs_1.vu_3$ , which does not exhibit a subduction jump at sur-

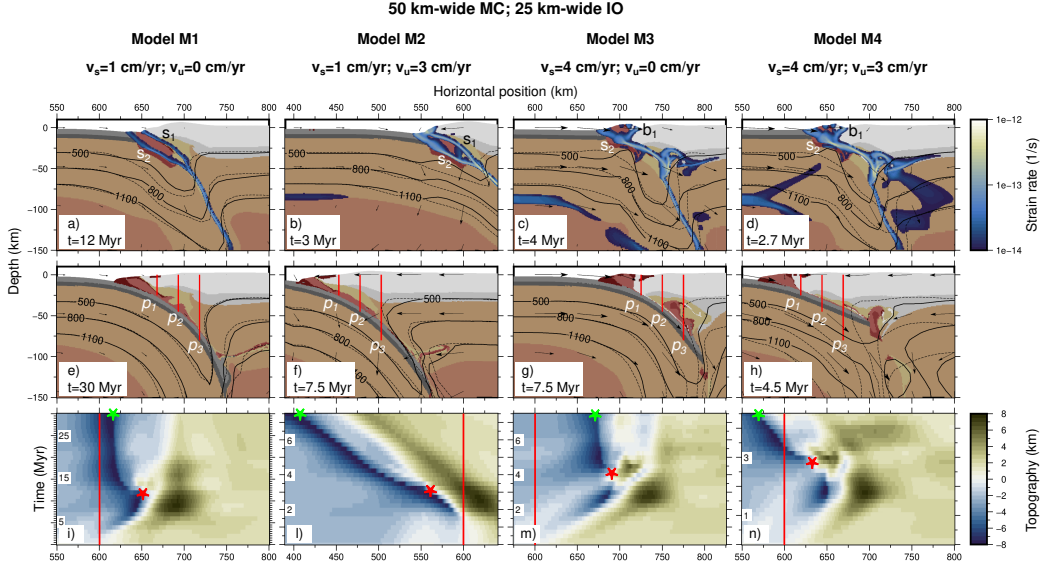


**Figure 6.** The evolution of models with a 50 km-wide microcontinent (MC) and a 25 km-wide inner ocean (IO) at two distinct stages, including velocity fields and strain rates (panels a-h), and the evolution of topography throughout the entire duration of simulations (panels i-n) are presented for different velocities of the subducting plate ( $v_s$ ) and the upper plate ( $v_u$ ). Red lines on panels a-d ( $p_1$ ,  $p_2$ , and  $p_3$ ) indicate the position of the thermal profiles shown in Fig. 7.  $s_1$  indicates the first subduction channel and  $s_2$  the second subduction channel after the subduction jump.  $b_1$  indicates the back thrust fault inside the accretionary wedge. Black lines indicate 500, 800 and 1100 °C isotherms, while dashed black lines indicate the same isotherms referred to NM models. Background colors define the composition as in Fig. 1. In panels i-n, red lines and red stars indicate the initial position and the maximum advancement of the trench, respectively, while the green stars indicate the maximum retreat of the trench.

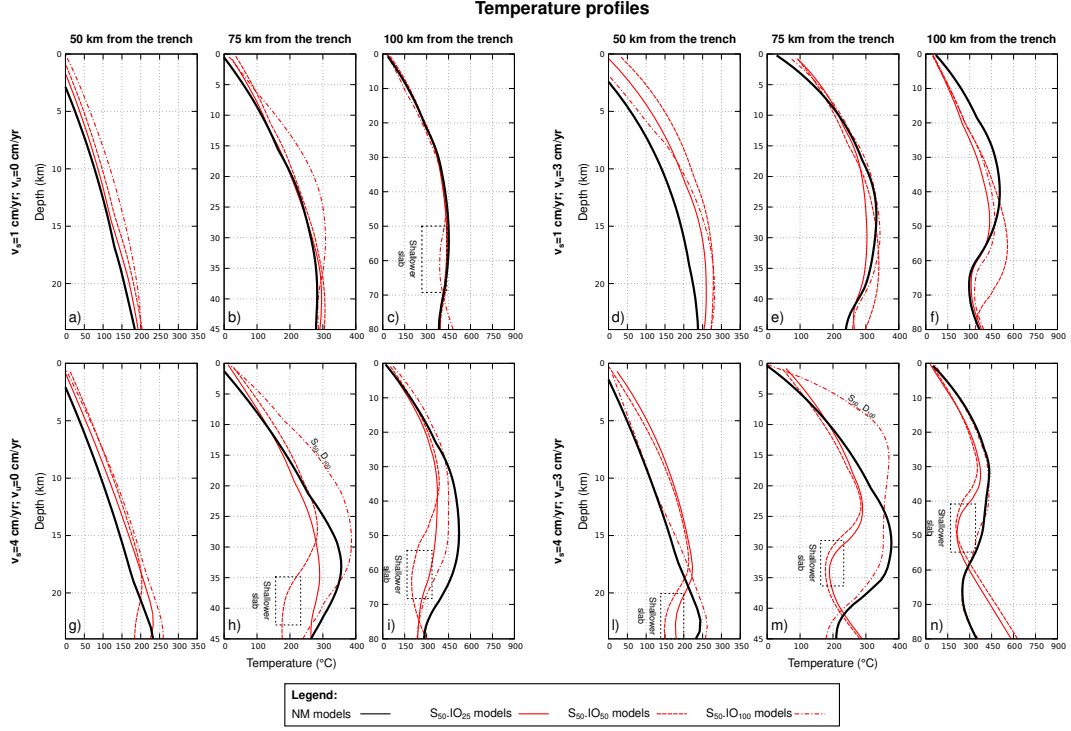


**Figure 7.** Temperature profiles for models with 50 km-wide microcontinent at different distances from the trench: 50 km (panels a, d, g, and l), 75 km (panels b, e, h, and m), and 100 km (panels c, f, i and, n). Continuous black lines indicate the profiles of models without microcontinents (NM). Continuous red lines indicate models with 25 km-wide inner ocean, dashed lines indicate models with 50 km-wide inner ocean, and dashed-dotted lines indicate models with 100 km-wide inner ocean.

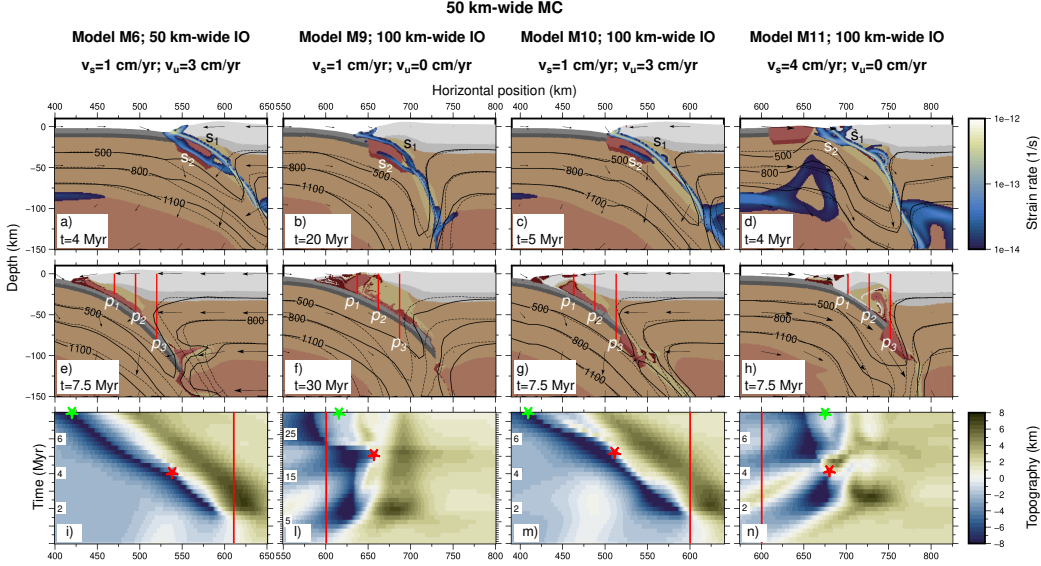


**Figure 8.** The evolution of models with a 50 km-wide microcontinent (MC), 50 (panels a and e) and 100 (panels b-d and f-h) km-wide inner ocean (IO), at two distinct stages, including velocity fields and strain rates, and the evolution of topography throughout the entire duration of simulations (panels i-n) are presented for different velocities of the subducting plate ( $v_s$ ) and the upper plate ( $v_u$ ). Red lines on panels a-d ( $p_1$ ,  $p_2$ , and  $p_3$ ) indicate the position of the thermal profiles shown in Fig. 7.  $s_1$  indicates the first subduction channel and  $s_2$  the second subduction channel after the subduction jump. Black lines indicate 500, 800 and 1100 °C isotherms, while dashed black lines indicate the same isotherms referred to NM models. Background colors define the composition as in Fig. 1. In panels i-n, red lines and red stars indicate the initial position and the maximum advancement of the trench, respectively, while the green stars indicate the maximum retreat of the trench.

500 face. Instead, the detachment between the upper and lower continental crust of the micro-  
 501 continent occurs deep in the subduction channel (from  $s_1$  to  $s_2$  in Fig. 8a and Movie  
 502 S8 in the Supporting Information). However, the detachment occurs when the micro-  
 503 continent is still shallow and, as a consequence, the larger amount of continental material  
 504 in the inner portion of the wedge (Fig. 8e) determines the increases of temperature  
 505 by up to 100°C due to the higher radiogenic energy produced (dashed red line in Fig.  
 506 7d). On the contrary, the increase in temperatures in the deeper and farther portion of  
 507 the mantle wedge (7e and f) is attributed to the steep slab, compared to models with-  
 508 out a microcontinent.

509 Conversely, an inner ocean of 100 km allows for more continuous subduction for  
 510 all velocities considered (M9-M12 in Fig. 8b, c and d), without accretion of the micro-  
 511 continent at the trench (Fig. 8f, g and h). Models  $M9_{50.IO_{100}.v_{s1}.v_{u0}}$  and  $M10_{50.IO_{100}.v_{s1}.v_{u3}}$   
 512 exhibit a similar behavior, characterized by the detachment between the upper and lower  
 513 continental crust of the microcontinent deep in the subduction channel (from  $s_1$  to  $s_2$   
 514 in Fig. 8b and c), favoring the recycling and exhumation of subducted material from the  
 515 microcontinent at the end of the evolution (Fig. 8f and g).

516 However, model M9 is characterized by a larger amount of recycled material due  
 517 to the slower velocities in the mantle wedge, allowing for a wider area in which subducted  
 518 material can be exhumed. Specifically, in model M9, there is exhumation up to 75 km

519 from the trench (profile  $p_2$  in Fig. 8f), while in model M10, the recycling is limited to  
 520 50 km from the trench (profile  $p_1$  in Fig. 8g). As a result, model M9 shows a higher tem-  
 521 perature increase (approximately 80 °C) along geotherm75 (dotted-dashed red line in Fig.  
 522 7b), whereas model M10 is characterized by a similar increase in temperatures along geotherm50  
 523 (dotted-dashed red lines in Fig. 7d) and a decrease in temperature along geotherm100,  
 524 as observed in models with a narrower inner ocean (red lines in Fig. 7f).

525 The push of the exhumed material against the accretionary wedge causes a sud-  
 526 den retreat of the trench, more noticeable in model M9, due to the larger amount of ex-  
 527 humed microcontinent (red stars in Fig. 8l and m). A similar behavior can also be ob-  
 528 served by comparing models  $M11_{50}.IO_{100}.vs_4.vu_0$  and  $M12_{50}.IO_{100}.vs_4.vu_3$ . Both mod-  
 529 els are characterized by the final upwelling of subducted material between 75 and 100  
 530 km from the trench (Fig. 8h), resulting in a remarkable temperature increase of approx-  
 531 imately 100 °C along geotherm75 (dotted-dashed red lines in Fig. 7h and m). The only  
 532 difference is observed at the trench before the collision of the microcontinent, where model  
 533 M11 shows a jump of the subduction in front of the microcontinent (from  $s_1$  to  $s_2$  in Fig.  
 534 8d, red star in Fig. 8n and Movie S9 in the Supporting Information), while model M12  
 535 displays a continuous subduction.

### 536 3.4 Models with 75 km-wide microcontinent - models L

#### 537 3.4.1 Models with 25 km-wide inner ocean - models L1-L4

538 The introduction of a 75 km-wide microcontinent relatively close to the upper plate  
 539 (25 km-wide inner ocean) does not significantly impact the evolution of models with low  
 540 velocity of the subducting plate ( $L1_{75}.IO_{25}.vs_1.vu_0$  and  $L2_{75}.IO_{25}.vs_1.vu_3$ ) compared  
 541 to models with smaller microcontinents (M1 and M2). In these models, there is still a  
 542 jump of the subduction inside the microcontinent, resulting in the accretion of part of  
 543 the microcontinent at the trench and limited recycling at the end of the evolution of the  
 544 previously subducted portion of the microcontinent.

545 On the contrary, models with a faster upper plate (models  $L3_{75}.IO_{25}.vs_4.vu_0$  and  
 546  $L4_{75}.IO_{25}.vs_4.vu_3$ ) exhibit higher resistance to the subduction of the microcontinent com-  
 547 pared to models with the same subduction velocity but smaller microcontinents (M3 and  
 548 M4). In particular, model L3 is characterized by the interruption of the subduction as-  
 549 sociated with the development of a back thrust fault behind the accretionary wedge ( $s_1$   
 550 and  $b_1$  in Fig. 9a, respectively). However, unlike model M3, the subduction does not restart  
 551 along a new subduction channel, and the final setting resembles that of a typical con-  
 552 tinental collision (Fig. 9c and Movie S10 in the Supporting Information). As a conse-  
 553 quence, the topography does not feature a deep and narrow trench, and the oceanic basin  
 554 advances continuously throughout the evolution (Fig. 9e).

555 Similarly, the initial phase of the evolution of model L4 resembles that of model  
 556 M4, both characterized by the interruption of subduction and the development of a back  
 557 thrust fault ( $b_1$  in Fig. 9b and model M4 in Fig. 6d). However, in this case, the inter-  
 558 ruption of subduction lasts longer, and the development of a new subduction that sep-  
 559 arates the microcontinent ( $s_2$  in Fig. 9b) occurs with a 1 Myr delay compared to M4,  
 560 resulting in a more prolonged period of inactive subduction (Fig. 9f and Movie S11 in  
 561 the Supporting Information). Nonetheless, the final configuration is very similar between  
 562 models M4 and L4, both mechanically (compare Fig. 6g and Fig. 9d) and thermally (com-  
 563 pare continuous red and yellow lines in Fig. 10l-n).

#### 564 3.4.2 Effects of wider inner oceans - models L5-L12

565 For these models, an inner ocean of 50 km allows the subduction of the microcon-  
 566 tinent only in the case of high subduction velocity and a fixed upper plate (model  $L7_{75}.IO_{50}.vs_4.vu_0$ ),  
 567 while no significant differences can be observed for all the other velocities considered. In

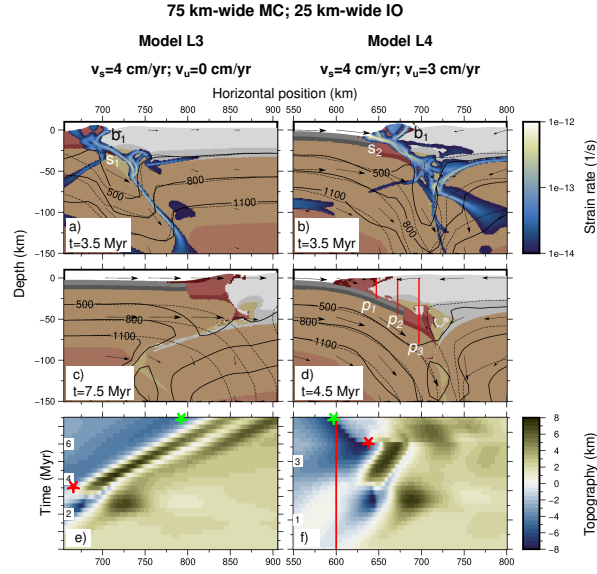


**Figure 9.** The evolution of models with a 75 km-wide microcontinent (MC) and a 25 km-wide inner ocean (IO) at two distinct stages, including velocity fields and strain rates (panels a-d), and the evolution of topography throughout the entire duration of simulations (panels e and f) are presented for different velocities of the subducting plate ( $v_s$ ) and the upper plate ( $v_u$ ). Red lines on panels d ( $p_1$ ,  $p_2$ , and  $p_3$ ) indicate the position of the thermal profiles shown in Fig. 10.  $s_1$  indicates the first subduction channel and  $s_2$  the second subduction channel after the subduction jump.  $b_1$  indicates the back thrust fault inside the accretionary wedge. Black lines indicate 500, 800 and 1100 °C isotherms, while dashed black lines indicate the same isotherms referred to NM models. Background colors define the composition as in Fig. 1. In panels e and f, red lines and red stars indicate the initial position and the maximum advancement of the trench, respectively, while the green stars indicate the maximum retreat of the trench.

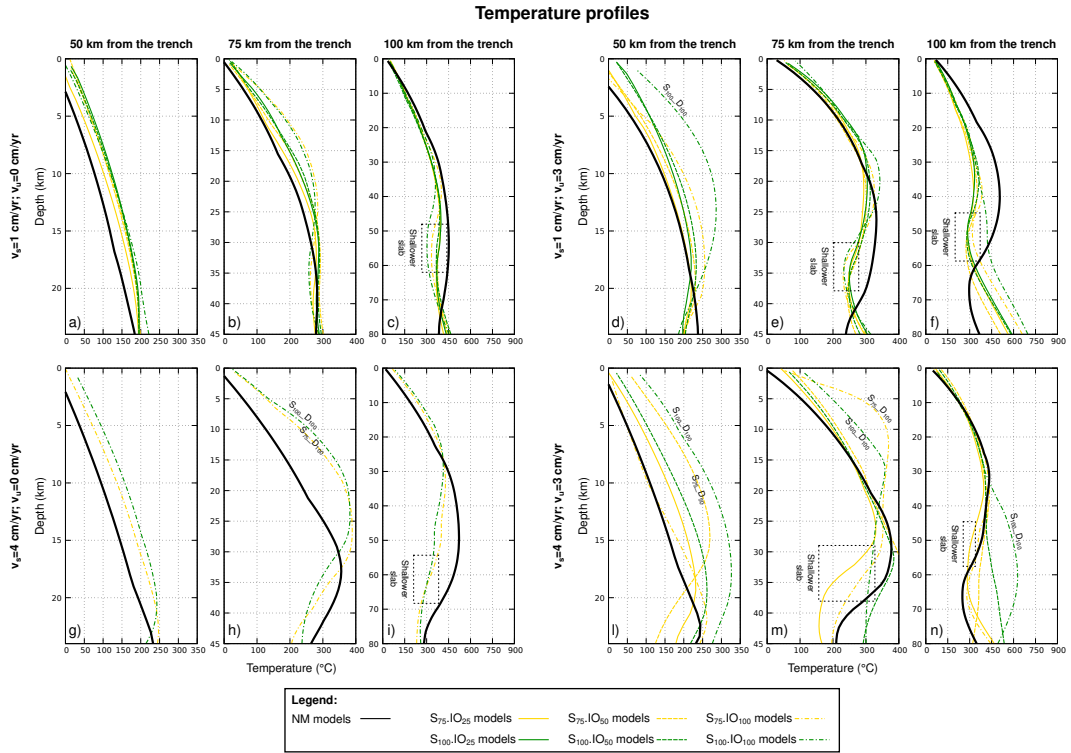


**Figure 10.** Temperature profiles at different distances from the trench: 50 km (panels a, d, g, and l), 75 km (panels b, e, h, and m), and 100 km (panels c, f, i and, n). Continuous black lines indicate the profiles of models without microcontinents (NM). Yellow lines indicate models with 75 km-wide microcontinent and dark green lines indicate models with 100 km-wide microcontinent. Continuous colored lines indicate models with 25 km-wide inner ocean, dashed colored lines indicate models with 50 km-wide inner ocean, and dashed-dotted colored lines indicate models with 100 km-wide inner ocean.

particular, model L7 is still characterized by both the interruption of subduction and the development of a back thrust fault behind the accretionary wedge ( $s_1$  and  $b_1$ , respectively, in Fig. 11a). However, in this case, subduction is able to restart inside the microcontinent after approximately 2 Myr, similar to that observed for model L4, and the final setting is characterized by the accretion at the trench of a part of the microcontinent (Fig. 11d). The long interruption of subduction does not allow the development of a long slab at the end of the evolution, making it impossible to observe recycling in the wedge or to thermally compare this model with the model without a microcontinent.

A wider inner ocean (100 km) does not clearly affect the evolution of models with a low velocity of the subducting plate (models  $L9_{75}.IO_{100}.vs_1.vu_0$  and  $L10_{75}.IO_{100}.vs_1.vu_3$ ), which, once again, show a jump of subduction backward of the microcontinent, with the consequent accretion of part of the microcontinent at the trench (see models M1 and M2 in Fig. 6a, b, e, and f). Conversely, models  $L11_{75}.IO_{100}.vs_4.vu_0$  and  $L12_{75}.IO_{100}.vs_4.vu_3$  are characterized by the continuous subduction of the microcontinent. Although the final setting of these two models is very similar, showing both no accretion and recycling of subducted material at approximately 75-100 km from the trench (between profiles  $p_2$  and  $p_3$  in Fig. 11e and f), the dynamics differs before the collision of the microcontinent. Model L11 is characterized by the jump of the subduction channel in front of the microcontinent (from  $s_1$  to  $s_2$  in Fig. 11b), while model L12 shows a continuous subduction channel throughout the entire evolution ( $s_1$  in Fig. 11c). The upwelling of subducted continental material from a maximum depth of approximately 50-60 km determines both a slight trench retreat (seen between red and green stars in Fig. 11h and i) and an increase in temperature compared to models NM3 and NM4 along geotherm<sub>75</sub> (dashed-dotted yellow lines in Fig. 10h and m).

### 3.5 Models with 100 km-wide microcontinent - models XL

Models with a 100 km-wide microcontinent exhibit a similar evolution to those observed in models with a 75 km-wide microcontinent, despite the larger dimension allowing for a greater amount of accreted material at the trench and increased recycling of subducted material. For example, in model  $XL1_{100}.IO_{25}.vs_1.vu_0$ , we observe a jump in subduction (from  $s_1$  to  $s_2$  in Fig. 12a), similar to what is seen in models L1 and M1 (Fig. 6a and e). However, the larger microcontinent size allows for the accretion of a greater amount of material at the trench, and, simultaneously, recycling of subducted material can be observed from a greater depth, approximately 70 km (between profiles  $p_2$  and  $p_3$  in Fig. 12e and Movie S12 in the Supporting Information). A similar behavior is observed in model  $XL2_{100}.IO_{25}.vs_1.vu_3$ . In contrast, in models  $XL3_{100}.IO_{25}.vs_4.vu_0$  and  $XL4_{100}.IO_{25}.vs_4.vu_3$ , subduction is interrupted after the collision of the microcontinent, similar to the observation in model L3 (Fig. 9a and c).

Similar to observations in models with 75 km-wide microcontinents, a wider inner ocean facilitates the subduction of the microcontinent. In models  $XL7_{100}.IO_{50}.vs_4.vu_0$  and  $XL8_{100}.IO_{50}.vs_4.vu_3$ , after the collision of the microcontinent, the subduction restarts with the development of a new subduction channel just before the end of the evolution ( $s_1$  in Fig. 12b and f). Lastly, a 100 km-wide inner ocean allows for a more continuous subduction after the collision of the microcontinent in models  $XL11_{100}.IO_{100}.vs_4.vu_0$  and  $XL12_{100}.IO_{100}.vs_4.vu_3$ , with no observed accretion at the trench (Fig. 12g and h). However, model XL11 is characterized by a jump of the subduction channel in front of the microcontinent, (from  $s_1$  to  $s_2$  in Fig. 12c), while model XL12 shows a continuous subduction throughout the entire evolution ( $s_1$  in Fig. 12d). In these models, the subduction of the entire microcontinent results in the recycling of continental material between 75 and 100 km from the trench, from a depth of approximately 50 km (between profiles  $p_2$  and  $p_3$  in Fig. 12g and h). The upwelling of material determines an increase in temperature of the mantle wedge with respect to model without microcontinent, in particular along the geotherm<sub>75</sub> of model XL11 (dashed-dotted green line in Fig. 10h)

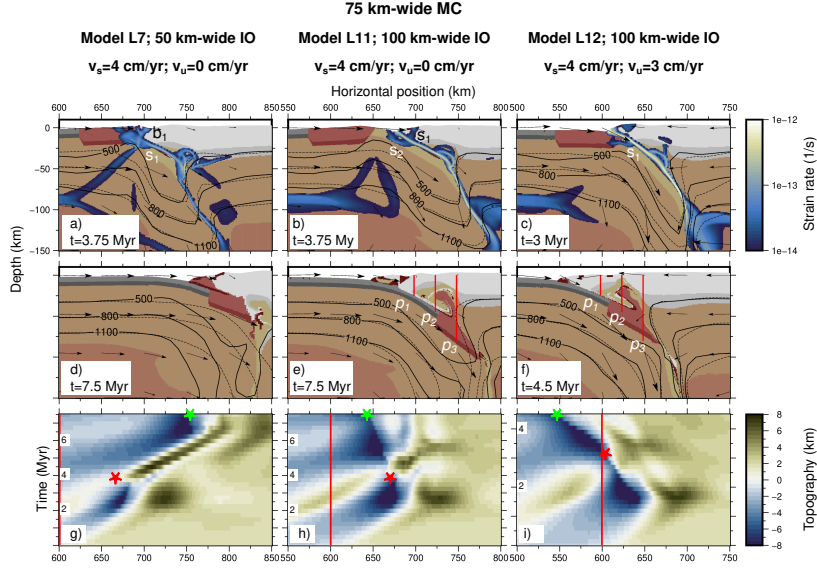


**Figure 11.** The evolution of models with a 75 km-wide microcontinent (MC) and a 50 (panels a and d) and 100 (panels b-c and e-f) km-wide inner ocean (IO) at two distinct stages, including velocity fields and strain rates (panels a-f), and the evolution of topography throughout the entire duration of simulations (panels g-i) are presented for different velocities of the subducting plate ( $v_s$ ) and the upper plate ( $v_u$ ). Red lines on panels a-d ( $p_1$ ,  $p_2$ , and  $p_3$ ) indicate the position of the thermal profiles shown in Fig. 10.  $s_1$  indicates the first subduction zone and  $s_2$  the second subduction zone after the subduction jump.  $b_1$  indicates the back thrust fault inside the accretionary wedge. Black lines indicate 500, 800 and 1100 °C isotherms, while dashed black lines indicate the same isotherms referred to NM models. Background colors define the composition as in Fig. 1. In panels g-i, red lines and red stars indicate the initial position and the maximum advancement of the trench, respectively, while the green stars indicate the maximum retreat of the trench.

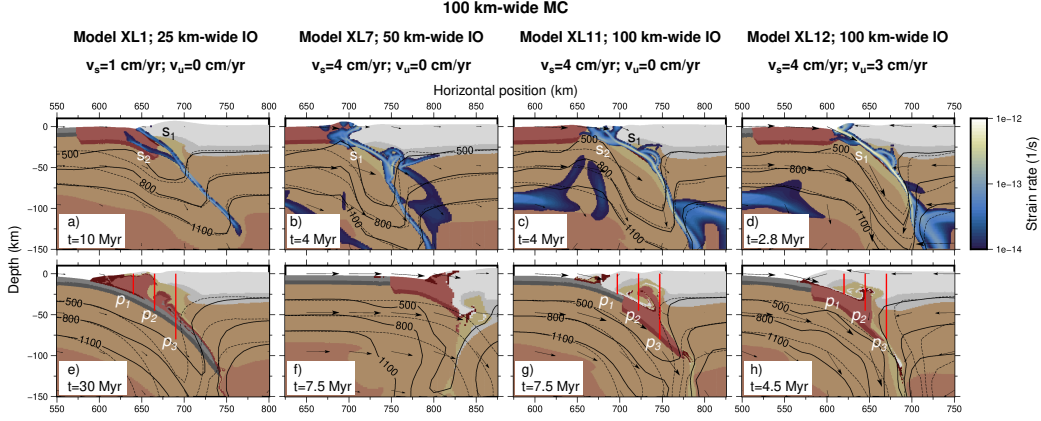


**Figure 12.** The evolution of models with a 100 km-wide microcontinent (MC) and a 25 (panels a and e), 50 (panels b and f), and 100 (panels c, d, g and h) km-wide inner ocean (IO) at two distinct stages, including velocity fields and strain rates are presented for different velocities of the subducting plate ( $v_s$ ) and the upper plate ( $v_u$ ). Red lines on panels e-d ( $p_1$ ,  $p_2$ , and  $p_3$ ) indicate the position of the thermal profiles shown in Fig. 10.  $s_1$  indicates the first subduction zone and  $s_2$  the second subduction zone after the subduction jump. Black lines indicate 500, 800 and 1100 °C isotherms, while dashed black lines indicate the same isotherms referred to NM models. Background colors define the composition as in Fig. 1.

620 and along all the geotherms calculated for model XL12 (dashed-dotted green lines in Fig.  
621 10l-n).

## 622 4 Discussion

623 In this section, we first discuss the effects of plate velocities on subduction systems  
624 without microcontinents. Subsequently, we delve into the results regarding the mechan-  
625 ical impact (including accretion/subduction, slab geometry, and recycling) of microcon-  
626 tinent with varying sizes. We aim to compare our findings with previous research while  
627 placing special emphasis on thermal effects and their potential implications for the meta-  
628 morphic conditions of recycled material. Finally, we briefly discuss our results in the con-  
629 text of different geodynamic reconstructions.

### 630 4.1 Impact of plate velocities on subduction systems without microcon- 631 tinents

632 The evolution of our reference model without a microcontinent and low convergence  
633 velocity ( $v_s=1 \text{ cm yr}^{-1}$  and  $v_u=0 \text{ cm yr}^{-1}$ ) represents the typical progression of an ocean-  
634 continent subduction system. This system is characterized by the localization of high  
635 strain rates along the plate interface, eventually forming a continuous subduction chan-  
636 nel from the surface to the asthenospheric mantle.

637 The low velocity imposed on the subducting plate does not lead to significant cou-  
638 pling between the plates, resulting in a lack of high strain rates within the continental  
639 crust of the upper plate. Consequently, its deformation is restricted to the development  
640 of topographical height after a few million years of evolution, which tends to collapse over  
641 time. Moreover, the low coupling between the plates results in a lack of ablation of con-  
642 tinental material from the upper plate.

643 The increase in the convergence velocity induces different behaviors depending on  
 644 the velocities imposed on both the subducting and upper plates. In fact, the model with  
 645 total convergence of  $4 \text{ cm yr}^{-1}$  and a faster upper plate ( $v_s=1 \text{ cm yr}^{-1}$  and  $v_u=3 \text{ cm yr}^{-1}$ )  
 646 has a similar evolution of the model with  $v_s=1 \text{ cm yr}^{-1}$  and the fixed upper plate, be-  
 647 ing characterized by low strain rates in the upper plate and lack of ablation.

648 On the contrary, the model with the same total convergence but with the entire  
 649 velocity imposed on the subducting plate ( $v_s=4 \text{ cm yr}^{-1}$  and  $v_u=0 \text{ cm yr}^{-1}$ ) shows higher  
 650 coupling between the plates. This results in the development of both high strain rate bands  
 651 and increased topography in the upper plate. Additionally, this model displays ablation  
 652 of continental material from both the upper and lower crusts of the upper plate, lead-  
 653 ing to recycling in the mantle wedge. A similar behavior is observed when increasing the  
 654 velocity of the upper plate in the case of a total convergence of  $7 \text{ cm yr}^{-1}$ .

655 Therefore, our models demonstrate that the overall evolution of a subduction sys-  
 656 tem is primarily controlled by the velocity of the subducting plate, leading to increased  
 657 deformation of the upper plate at higher velocities. In contrast, different velocities of the  
 658 upper plate have secondary effects on the evolution.

659 This finding is significant in the context of geodynamic reconstructions, where nu-  
 660 merical simulations typically involve velocities imposed only on the subducting plate to  
 661 replicate the total convergence between plates. However, our results indicate that the  
 662 large-scale dynamics of subduction systems are not solely influenced by the total con-  
 663 vergence velocity but also by the distribution of velocities on the two plates, even when  
 664 the total convergence velocities are the same.

## 665 **4.2 Impact of microcontinents on an ocean-continent subduction sys-** 666 **tem**

### 667 **4.2.1 Type of subduction**

668 We analyzed whether the presence of microcontinents with varying dimensions, sit-  
 669 uated at different distances from the trench, impacts the evolution of an ocean-continent  
 670 subduction system. Our models indicate that predicting the subduction occurrence and  
 671 patterns of microcontinents is challenging, as they depend on multiple factors that can-  
 672 not be known a priori. However, general trends can be identified concerning the dimen-  
 673 sions of both the microcontinent and the inner ocean, as well as the velocities of both  
 674 the subducting and upper plates.

675 Our results indicate that continuous subduction can occur regardless of both the  
 676 plate velocities and the inner ocean dimension, as long as small microcontinents are con-  
 677 sidered (i.e., 25 km; bottom row of Fig. 13). Consequently, none of these models exhibit  
 678 accretion of continental material at the trench. Therefore, the accretionary wedge is formed  
 679 solely by sediments produced at the trench.

680 On the contrary, the behavior of a subduction system in case of larger microcon-  
 681 tinents ( $>25 \text{ km}$ ) depends both on the plate velocities and the dimension of the inner  
 682 ocean. In general, an inner ocean larger than the microcontinent favors the development  
 683 of a continuous subduction, often characterized by subduction of crustal material with-  
 684 out accretion (green and yellow squares without 'A' in Fig. 13). However, a distinct dif-  
 685 ference is observed between models with low ( $v_s=1 \text{ cm yr}^{-1}$ ) and high ( $v_s=4 \text{ cm yr}^{-1}$ )  
 686 velocities of the subducting plate. Models with a low subducting plate velocity ( $v_s=1$   
 687  $\text{cm yr}^{-1}$ ) are characterized by a continuous subduction, often with a jump in the sub-  
 688 duction channel (yellow squares in Fig. 13). In fact, a continuous subduction can be ob-  
 689 served only for models with 50 km-wide microcontinents and medium-large inner oceans  
 690 (75-100 km), in relation to different velocities of the upper plate (green squares in Fig.  
 691 13). In contrast, models characterized either by 50 km-wide microcontinent and narrow

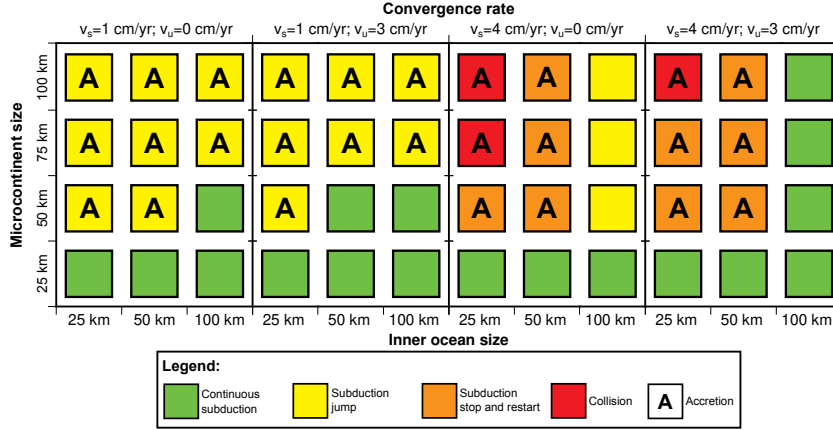


**Figure 13.** Different type of subduction observed. Green squares indicate models characterized by a continuous subduction; yellow squares indicate models in which the subduction is not interrupted but a jump of the subduction channel is observed; orange squares indicate models characterized by an interruption and a restart of the subduction along a new subduction channel; red squares indicate continental collision. Models with an 'A' are characterized by accretion of the microcontinent at the trench.

692 inner oceans, or by 75 and 100 km-wide microcontinent always show a jump in the sub-  
 693 duction channel ('A' yellow squares in the top two lines of  $v_s=1 \text{ cm yr}^{-1}$  models in Fig.  
 694 13). The jump of the channel occurs behind the microcontinent when the microconti-  
 695 nent has been partially subducted, leading to detachment between the upper and lower  
 696 crust. This behavior promotes accretion at the trench of part of the upper crust of the  
 697 microcontinent ('A' yellow squares in Fig. 13), while another part is recycled in the man-  
 698 tle wedge. However, recycling in these models is limited due to the small amount of sub-  
 699 duced material.

700 Differently, models with  $v_s=4 \text{ cm yr}^{-1}$  and 25-50 km-wide inner oceans show an  
 701 interruption of the subduction when the microcontinents collide, with the consequent  
 702 development of back thrust faults inside the upper plate (orange and red squares in Fig.  
 703 13). In most cases the subduction restarts along a new subduction channel locate within  
 704 the microcontinent, with consequent accretion of the microcontinent at the trench ('A'  
 705 orange squares in Fig. 13) and partial subduction and recycling of continental material.  
 706 However, the restart does not occur in case of larger microcontinents and narrower in-  
 707 ner oceans, and the models are characterized by a final setting typical of continental col-  
 708 lision (red squares in Fig. 13), similar to what previously observed by Tao et al. (2020).  
 709 Nonetheless, a 100 km-wide inner ocean eases the subduction, with differences related  
 710 to the velocity of the upper plate. In fact, a continuous subduction without jump of the  
 711 channel can be observed for  $v_u=3 \text{ cm yr}^{-1}$  (green square in the last column in Fig. 13),  
 712 while a subduction jump characterized the models with a fixed upper plate (yellow square  
 713 without 'A' in Fig. 13). However, in this case the jump occurs before the collision of the  
 714 microcontinent and the new subduction channel restart in front of it, therefore avoid-  
 715 ing accretion of the microcontinent at the trench.

716 Therefore, our results show a direct dependence between the size of microcontinents,  
 717 the size of the inner ocean, and the capability to be subducted or accreted. In general,  
 718 a continuous subductions after the collision of the microcontinent does not occur if the  
 719 microcontinent is wider than the size of the inner ocean, i.e. its distance from the trench.  
 720 This correlation between size and initial distance of the microcontinent from the upper  
 721 plate is in agreement with Yan et al. (2022), even if they considered larger microconti-

722 nents located further from the trench. In addition, higher velocities imposed on the sub-  
 723 ducting plates increase the coupling between the plates that results in greater difficul-  
 724 ties to produce a continuous subduction or, in some cases, to subduct at all the micro-  
 725 continent. On the contrary, higher velocities imposed on the upper plate ease the sub-  
 726 duction of the microcontinent, as previously observed by Yang et al. (2018), and, in fact,  
 727 all models with a 100 km-wide ocean and  $v_u=3 \text{ cm yr}^{-1}$  are not characterized neither  
 728 by interruption of the subduction nor jump of the subduction channel throughout their  
 729 entire evolution.

730 All the various types of subduction we observed in our models (continuous subduc-  
 731 tion, jump of the subduction channel and collision) can be well compared to what ob-  
 732 served in previous studies (Tetreault & Buitter, 2012; Vogt & Gerya, 2014; Yang et al.,  
 733 2018), even if both different initial setup and different parameters for both rheology and  
 734 initial boundary conditions were adopted. For example, either plateau subduction, un-  
 735 derplating and basal accretion, or frontal accretion observed by Vogt and Gerya (2014)  
 736 can be compared either to continuous subduction, jump of the subduction channel with  
 737 both accretion and subduction, or collision of the microcontinent predicted by our mod-  
 738 els. Similarly, the evolution observed by Tetreault and Buitter (2012) in case of either ho-  
 739 mogeneous microcontinents or basal/middle detachment match either tha continuous sub-  
 740 duction or the jump of the subduction channel noticed in our models.

741 In addition, the jump of the subduction channel has been hypothesized for geody-  
 742 namic reconstructions in different convergent margins. For example, in the reconstruc-  
 743 tion of the evolution of the Sesia-Lanzo Zone in the western Alps, Babist et al. (2006)  
 744 presented a kinematic model characterized by the collision of successive continental units  
 745 (i.e., microcontinents) that resulted in accretion at the trench and retreat of the subduc-  
 746 tion channel behind the microcontinents. A similar behavior has been presented by Peng  
 747 et al. (2022) in their reconstruction of the tectonic evolution of Central Tibet. They con-  
 748 sidered the collision of the microcontinent Amdo against Qiangtang, leading to the sub-  
 749 sequent jump of the subduction behind Amdo.

#### 750 **4.2.2 Slab geometry**

751 We examined the shallow slab dip (above 50 km depth) of all models to determine  
 752 if it depends the investigated parameters. Our models revealed a correlation between the  
 753 shallow slab dip and the presence and dimensions of the introduced microcontinents in  
 754 the domain (Fig. 14). Specifically, we observed a linear decrease in the slab dip for wider  
 755 microcontinents, with a linear correlation coefficient of  $r=-0.65$  (indicated by the black  
 756 line in Fig. 14), resulting in a variation of up to  $10^\circ$  between models with 25 km-wide  
 757 and 100 km-wide microcontinents (Fig. 14). In contrast, the shallow slab dip does not  
 758 appear to be directly correlated with either the dimensions of the inner ocean or the ve-  
 759 locities of the plates, as already observed by Lallemand et al. (2005) and Roda et al. (2011).

760 On the contrary, the deep geometry of the slab seems unrelated to the size of the  
 761 microcontinent but is closely tied to the velocities of the plates. All models exhibit a ver-  
 762 ticalization of the slab above 100 km deep, except for models with an upper plate mov-  
 763 ing faster than the subducting plate ( $v_s=1 \text{ cm yr}^{-1}$  and  $v_u=3 \text{ cm yr}^{-1}$ ). For these mod-  
 764 els, two distinct behaviors can be observed: in the case of 25 or 50 km-wide microcon-  
 765 tinents, the models are characterized by a horizontalization of the slab at approximately  
 766 200 km deep, while for larger microcontinents (i.e., 75 and 100 km), the slab does not  
 767 exhibit any variation in slab dip.

#### 768 **4.2.3 Recycling in the mantle wedge**

769 Different plate velocities influence the occurrence and style of crustal recycling in  
 770 the mantle wedge, as illustrated in Fig. 15, where black arrows indicate whether recy-

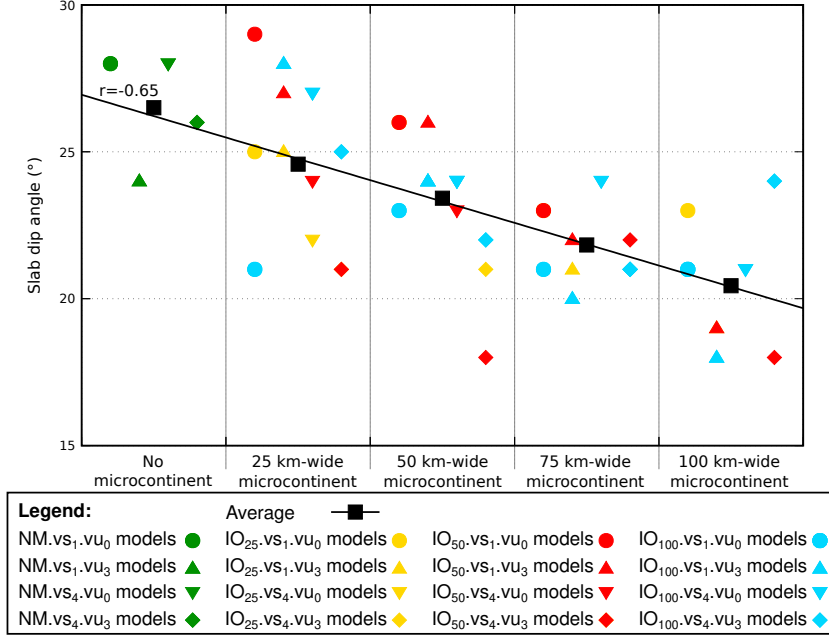


**Figure 14.** Shallow slab dip angle of all models in relation to the dimension of the microcontinent. Dark green indicate models without microcontinent; yellow, red and light blue indicate models with 25, 50 and 100 km-wide inner oceans, respectively. Different shapes indicate different velocities imposed on the plates. Black squares indicate the average dip for different dimension of the microcontinent and the black line represents the linear correlation.

771 cling of subducted material occurs for each model in different portions of the wedge at  
 772 distances of 50, 75, and 100 km from the trench (left, central, and right colored rectan-  
 773 gles). Our results indicate that models with high velocities of the upper plate ( $v_u=3 \text{ cm yr}^{-1}$ )  
 774 are characterized by either the absence or a small amount of recycled material, particu-  
 775 larly when associated with a slow subducting plate ( $v_s=1 \text{ cm yr}^{-1}$ ). This is because the  
 776 intense mantle flow below the overriding plate pushes the subducted material against the  
 777 slab, preventing recycling. This behavior is more evident in models with 25 or 50 km-  
 778 wide microcontinents, showing scarce or null recycling in the case of  $v_u=3 \text{ cm yr}^{-1}$ , while  
 779 abundant recycling is predicted at different distances for fixed upper plate (compare black  
 780 arrows in the two bottom rows in Fig. 15). Furthermore, higher subducting velocities  
 781 move the recycling area away from the trench. Models with  $v_s=1 \text{ cm yr}^{-1}$  show recy-  
 782 cling at 50/75 km from the trench (left/central colored rectangles of each model, respec-  
 783 tively, in Fig. 15), while models characterized by faster subducting plates ( $v_s=4 \text{ cm yr}^{-1}$ )  
 784 exhibit recycling at 75/100 km from the trench (central/right colored rectangles of each  
 785 model, respectively, in Fig. 15). A farther distance from the trench also results in deeper  
 786 regions of recycling, making it more challenging to have upwelling up to the surface or  
 787 even to shallow levels of the crust. Finally, large microcontinents (75-100 km) generally  
 788 allow both a deep exhumation of the frontal portion of the microcontinent (from approx-  
 789 imately 60-70 km deep) and a shallow exhumation of the central/back portion of the mi-  
 790 crocontinent (from approximately 15-20 km deep) in the case of  $v_s=1 \text{ cm yr}^{-1}$ .

791 Therefore, the velocity of both plates and the size of a microcontinent are signif-  
 792 icant parameters to consider for better constraining geodynamic reconstruction in the  
 793 case of exhumed rocks characterized by contrasting maximum pressure recorded. The  
 794 recycling of subducted material also affects the dynamics of the trench. In fact, mod-

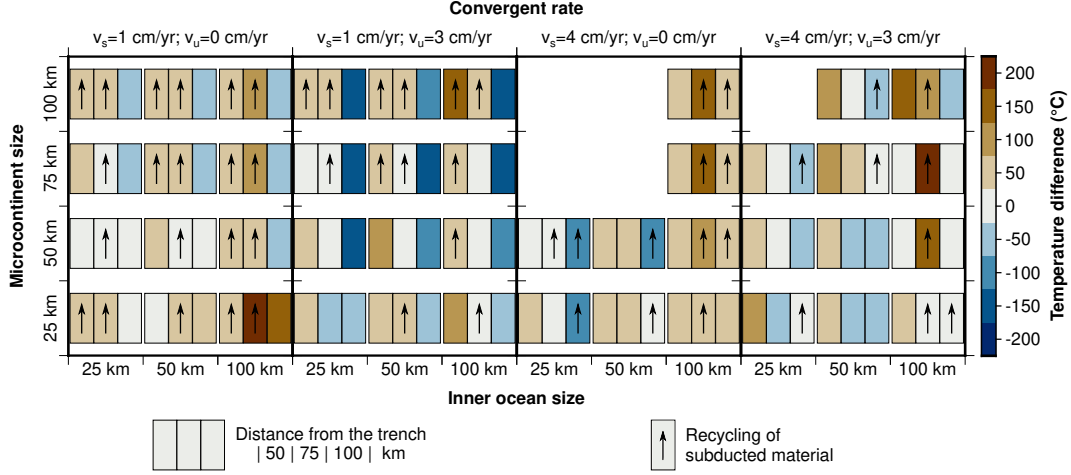


**Figure 15.** Temperature differences between each model and the equivalent models without microcontinent, calculated along geotherms located 50, 75 and 100 km far from the trench, as in Figs. 4, 7 and 10. Black arrows indicate areas characterized by exhumation of subducted material.

els with fast and abundant recycling are characterized by a clear trench retreat due to the push produced by the upwelling material toward the accretionary wedge.

#### 4.2.4 Thermal effects

We discuss the thermal effects due to a microcontinent in the subduction system with respect to equivalent models without microcontinents by comparing the geotherms at three different distances from the trench (50, 75, and 100 km) to separate the mantle wedge into three regions: inner, central, and outer (Fig. 15).

Our results show that the introduction of a microcontinent in a subduction system has a clear impact on the thermal state recorded in the mantle wedge, with different effects observed in different regions of the mantle wedge (Fig. 15). In particular, the inner portion of the wedge shows a general warming compared to models without a microcontinent (red left rectangles in Fig. 15), while the central and outer portions are characterized either by warming or cooling (red or blue central/right rectangles in Fig. 15) as a result of different mechanical evolution of the system.

Since the recycling of material in the inner portion of the wedge (left rectangles in Fig. 15) is limited to shallow levels, the warming in this area (approximately 50-100 °C for all models; white/light red left rectangles in Fig. 15) can be related to the heat flux produced by the recycling of deep material pushing toward the trench. However, no additional heat can be related to higher radiogenic energy produced because the placement of continental crust from the microcontinent, either by accretion or by shallow recycling, replaces similar existing continental crust of the upper plate.

Differently, recycling of continental material in the central and outer portions of the mantle wedge produces warming related both to higher radiogenic energy, because of the large amount of continental crust in the mantle, and to upwelling of deeper and hotter material. Consequently, since the dynamic inside the mantle wedge is strictly correlated to plate velocities and the size and location of the microcontinent (as explained in Section 4.2.3), all of these factors affect the final thermal state of the models. Therefore, models characterized by parameters that favor the subduction of a larger amount

823 of continental material from the microcontinent (i.e., low velocities of the subducting plate  
 824 or a large inner ocean) exhibit a warm central mantle wedge (up to 200 °C; central rect-  
 825 angles either in the left panel or in the last column of the third and fourth panels in Fig.  
 826 15), where the recycling, or even the exhumation up to the surface, is more abundant.  
 827 Similarly, models with larger microcontinents are characterized by an increase in tem-  
 828 perature up to 150-200 °C in the central portion of the wedge (dark red central rectan-  
 829 gles in the top two lines in Fig. 15), when a large amount of continental crust is subducted  
 830 (i.e., for a large inner ocean).

831 On the contrary, high velocity imposed on the upper plate determines less warm-  
 832 ing or even cooling of the mantle wedge (central rectangles in the central columns of the  
 833 second and fourth panels in Fig. 15) because of low crustal recycling in the mantle wedge  
 834 (as explained in Section 4.2.3). In addition, the recycling in the central and outer por-  
 835 tions of the wedge, even if scarce, prevents the mantle flow below the overriding plate  
 836 from reaching the mantle wedge, with a consequent lack of a significant source of heat.  
 837 In fact, models with a more intense mantle flow (high velocities of the upper plate) are  
 838 always characterized by cooling in the outer portion of the wedge, up to 150 °C (right  
 839 blue rectangles in the second and fourth panels in Fig. 15). In addition, the thermal state  
 840 in the most external portion of the wedge is also affected by the slab geometry because  
 841 a higher slab dip facilitates a more intense counterflow in the mantle wedge that results  
 842 in higher temperatures. Therefore, models with large microcontinents and high veloc-  
 843 ities of the upper plate further limit the mantle flow toward the wedge (as explained in  
 844 Section 4.2.2 for the correlation between microcontinent size and slab dip).

845 The assessment of temperature variations in the mantle wedge is crucial to deter-  
 846 mining whether continental material recycled in the wedge records low or high temper-  
 847 atures. Consequently, the metamorphism recorded by these rocks may range from Lawsonite-  
 848 bearing blueschist or eclogite facies conditions to HP granulites, depending on the mi-  
 849 crocontinent subduction setting. In general, we observed that recycling in the inner and  
 850 central portions of the wedge is associated with a significant warming, reaching up to  
 851 150-200 °C. This warming is of great importance because the recycled material in these  
 852 areas can be exhumed to the surface more easily. Therefore, the velocity of both plates  
 853 and the size of microcontinents and inner oceans are significant parameters to consider,  
 854 not only for their consequences on the mechanical evolution but also for their impact on  
 855 the thermal state of the subduction system. These factors have direct effects on geody-  
 856 namic reconstruction, especially in the case of exhumed rocks characterized by high tem-  
 857 peratures recorded during active subduction.

### 858 4.3 Limitations and Future Works

859 In this work, we mainly focus on variations in the size and location of the micro-  
 860 continent, as well as variations in the initial velocity boundary conditions imposed on  
 861 both plates. We evaluate their effects on the evolution of subduction. However, we did  
 862 not consider rheology variations for the different materials in this study. The effects of  
 863 rheology variations and different thicknesses of the microcontinent have been previously  
 864 analyzed in other works (e.g. Tetreault & Buitert, 2012; Vogt & Gerya, 2014), and they  
 865 were proven to have effects on the subductibility of microcontinents.

866 Additionally, we did not consider either melting or hydration inside the mantle wedge,  
 867 although both could have effects on the recycling of material and, therefore, on the fi-  
 868 nal thermal setting of the models. Future studies could expand upon the work presented  
 869 here by incorporating these aspects into the numerical code.

870 Similarly, we decided to use 2D models to explore in detail the effects of specific  
 871 parameters throughout the entire evolution of subduction systems. However, future stud-  
 872 ies could include 3D numerical models to simulate more complex tectonic settings.

873 Finally, future works could involve a detailed analysis of pressure-temperature-time  
874 (PTt) paths predicted by the models for subducted and exhumed particles. This would  
875 allow for a comparison with natural PTt paths observed in systems thought to have ex-  
876 perience subduction and/or collision of microcontinents.

## 877 5 Conclusions

878 In this work, we investigated the effect of different velocities imposed on both plates  
879 on the evolution of an ocean-continent subduction system. In particular, we also ana-  
880 lyzed whether the introduction of microcontinents, characterized by different sizes and  
881 initial distances from the trench, impacts the system's evolution.

882 The first significant result is that the dynamics of a subduction system, in the ab-  
883 sence of microcontinents, are not only influenced by the total convergence velocity, but  
884 different velocities imposed on both plates, even with the same convergent velocity, also  
885 impact the evolution. In general, we observed that an increase in the velocity of the sub-  
886 ducting plate leads to higher coupling between plates, resulting in the ablation of ma-  
887 terial from the upper plate, irrespective of the total convergence rate.

888 When microcontinents are introduced into the system, we observed four different  
889 styles of subduction that depend on the velocities of the plates and both the dimension  
890 and initial distance of the microcontinent from the upper plate. Specifically, our mod-  
891 els showed: 1) continuous subduction, 2) continuous subduction with a jump in the sub-  
892 duction channel, 3) interruption and restart of the subduction along a new subduction  
893 channel, and 4) continental collision. We noticed that the subduction of microcontinents  
894 becomes more challenging as their dimensions increase, favoring the jump or interrup-  
895 tion of subduction. On the contrary, a large inner ocean facilitates a continuous subduc-  
896 tion. Additionally, different velocities of the plates also affect the subduction style; high  
897 subducting velocities make the subduction of microcontinents more difficult, while high  
898 velocities of the upper plate make it easier.

899 The style of subduction has primary effects on the wedge dynamics, particularly  
900 on the amount of subducted material that recycles in the mantle wedge, resulting in dif-  
901 ferent thermal conditions. A fixed upper plate, especially if coupled with a slow subduc-  
902 ting plate, favors the exhumation of recycled material from different depths up to either  
903 shallow levels or the surface. This is significant because the upwelling to shallow depths  
904 increases the temperature in the inner and central portions of the mantle wedge, directly  
905 affecting the metamorphic conditions recorded by subducted and exhumed rocks dur-  
906 ing their evolution.

907 Finally, models with conditions that favor the (partial) subduction of large micro-  
908 continents are characterized by synchronous exhumation of rocks derived from different  
909 portions of the microcontinent. Therefore, these rocks could have experienced either high  
910 or low-pressure and temperature conditions during their evolution.

## 911 Open Research Section

912 A complete description of the numerical code FALCON used in this work with the  
913 results of the benchmarks performed to test the features implemented in the code can  
914 be found on the Zenodo online open access repository Regorda (2022).

915 Input files with properties of the materials and parameters used in this work and  
916 the complete data set with the output files in Paraview format (vtu) of all of the mod-  
917 els tested in this work can be found on the Zenodo online open access repository Regorda  
918 and Roda (2023).

919 **Acknowledgments**

920 All the figures were created with either Generic Mapping Tool (GMT) plotting software  
921 (Wessel & Smith, 1998, 2001) or Gnuplot using scientific color maps designed by Crameri  
922 (2018a), Crameri (2018b) and Crameri et al. (2020). This research was funded by PRIN  
923 2020: POEM-POligEnetic Mélanges: anatomy, significance and societal impact.

924 **Author Contributions**

925 Conceptualization - AR, MR; Formal analysis - AR; Investigation - AR; Method-  
926 ology - AR, MR; Software - AR; Validation - AR, MR; Visualization - AR, MR; Writ-  
927 ing - Original draft - AR, MR; Writing - Review & editing - AR, MR;

## References

- 928
- 929 Abera, R., van Wijk, J., & Axen, G. (2016). Formation of continental fragments:  
930 The tamayo bank, gulf of california, mexico. *Geology*, *44*(8), 595–598. doi: 10  
931 .1130/g38123.1
- 932 Afonso, J. C., & Zlotnik, S. (2011). The subductability of continental lithosphere:  
933 The before and after story. *Frontiers in Earth Sciences*, *4*, 53–86. doi: 10  
934 .1007/978-3-540-88558-0\_3
- 935 Alejano, L. R., & Bobet, A. (2012). Drucker-Prager criterion. *Rock Mechanics and*  
936 *Rock Engineering*, *45*(6), 995–999. doi: 10.1007/s00603-012-0278-2
- 937 Amestoy, P. R., Duff, I. S., L'Excellent, J.-Y., & Koster, J. (2001). A fully Asyn-  
938 chronous Multifrontal Solver using Distributed Dynamic Scheduling. *Society*  
939 *for Industrial and Applied Mathematics*, *23*(1), 15–41.
- 940 Amestoy, P. R., Guermouche, A., L'Excellent, J.-Y., & Pralet, S. (2006). Hybrid  
941 scheduling for the parallel solution of linear systems. *Parallel Computing*,  
942 *32*(2), 136–156. doi: 10.1016/j.parco.2005.07.004
- 943 Anderson, J. (1995). *Computational fluid dynamics*. McGraw-Hill.
- 944 Andrews, E. R., & Billen, M. I. (2009). Rheologic controls on the dynamics of slab  
945 detachment. *Tectonophysics*, *464*(1), 60–69. doi: 10.1016/j.tecto.2007.09.004
- 946 Arredondo, K. M., & Billen, M. I. (2016). The effects of phase transitions and com-  
947 positional layering in two-dimensional kinematic models of subduction. *Journal*  
948 *of Geodynamics*. doi: 10.1016/j.jog.2016.05.009
- 949 Babeyko, A. Y., & Sobolev, S. V. (2005). Quantifying different modes of the late  
950 Cenozoic shortening in the central Andes. *Geology*, *33*(8), 621–624. doi: 10  
951 .1130/G21126.1
- 952 Babist, J., Handy, M. R., Konrad-Schmolke, M., & Hammerschmidt, K. (2006). Pre-  
953 collisional, multistage exhumation of subducted continental crust: The Sesia  
954 Zone, western Alps. *Tectonics*, *25*(TC6008). doi: 10.1029/2005TC001927
- 955 Billen, M. I., & Hirth, G. (2007). Rheologic controls on slab dynamics. *Geochem.*  
956 *Geophys. Geosyst.*, *8*(8). doi: 10.1029/2007GC001597
- 957 Bollino, A., Regorda, A., Sabadini, R., & Marotta, A. M. (2022). From rifting to  
958 oceanization in the Gulf of Aden: Insights from 2D numerical models. *Tectono-*  
959 *physics*, *838*, 229483. doi: 10.1016/j.tecto.2022.229483
- 960 Braun, J., & Willett, S. D. (2013). A very efficient o(n), implicit and par-  
961 allel method to solve the stream power equation governing fluvial inci-  
962 sion and landscape evolution. *Geomorphology*, *180-181*, 170-179. doi:  
963 10.1016/j.geomorph.2012.10.008
- 964 Burov, E. B. (2011). Rheology and strength of the lithosphere. *Marine and*  
965 *Petroleum Geology*, *28*(8), 1402–1443. doi: 10.1016/j.marpetgeo.2011.05.008
- 966 Chopin, C. (1984). Coesite and pure pyrope in high-grade blue- schists of the West-  
967 ern Alps. *Contrib Mineral Petrol*, *86*, 107–118.
- 968 Chopin, C. (2003). Ultrahigh-pressure metamorphism: tracing continental crust into  
969 the mantle. *Earth and Planetary Science Letters*, *212*(1), 1-14. doi: 10.1016/  
970 S0012-821X(03)00261-9
- 971 Christensen, U. R., & Yuen, D. A. (1985). Layered convection induced by phase  
972 transitions. *Journal of Geophysical Research*, *90*(B12), 10291–10300. doi: 10  
973 .1029/JB090iB12p10291
- 974 Cloos, M. (1993). Lithospheric buoyancy and collisional orogenesis: Subduc-  
975 tion of oceanic plateaus, continental margins, island arcs, spreading ridges,  
976 and seamounts. *Geological Society of America Bulletin*, *105*(6), 715. doi:  
977 10.1130/0016-7606(1993)105<0715:LBACOS>2.3.CO;2
- 978 Cordonnier, G., Bovy, B., & Braun, J. (2019). A versatile, linear complexity algo-  
979 rithm for flow routing in topographies with depressions. *Earth Surface Dynam-*  
980 *ics*, *7*(2), 549–562. doi: 10.5194/esurf-7-549-2019
- 981 Cramer, F. (2018a). Geodynamic diagnostics, scientific visualisation and StagLab  
982 3.0. *Geoscientific Model Development*, *11*(6), 2541–2562. doi: 10.5194/gmd-11

- 983 -2541-2018
- 984 Cramer, F. (2018b). *Scientific colour-maps*. Zenodo. doi: 10.5281/zenodo.1243862
- 985 Cramer, F., Magni, V., Domeier, M., Shephard, G. E., Chotalia, K., Cooper, G., ...
- 986 Thielmann, M. (2020). A transdisciplinary and community-driven database
- 987 to unravel subduction zone initiation. *Nature Communications*, *11*, 3750. doi:
- 988 10.1038/s41467-020-17522-9
- 989 De Franco, R., Govers, R., & Wortel, R. (2008a). Dynamics of continental colli-
- 990 sion: influence of the plate contact. *Geophysical Journal International*, *174*(3),
- 991 1101–1120. doi: 10.1111/j.1365-246X.2008.03857.x
- 992 De Franco, R., Govers, R., & Wortel, R. (2008b). Nature of the plate contact and
- 993 subduction zones diversity. *Earth and Planetary Science Letters*, *271*, 245–253.
- 994 doi: 10.1016/j.epsl.2008.04.019
- 995 Donea, J., & Huerta, A. (2003). *Finite Element Methods for Flow Problems* (Vol. 1).
- 996 Wiley. doi: 10.1017/CBO9781107415324.004
- 997 Donea, J., Huerta, A., Ponthot, J.-P., & Rodríguez-Ferran, A. (2004). Arbitrary
- 998 Lagrangian–Eulerian Methods. In *Encyclopedia of computational mechanics*
- 999 (chap. 14). John Wiley & Sons, Ltd. doi: 10.1002/0470091355.ecm009
- 1000 Duretz, T., Gerya, T. V., & May, D. A. (2011). Numerical modelling of spontaneous
- 1001 slab breakoff and subsequent topographic response. *Tectonophysics*, *502*(1–2),
- 1002 244–256. doi: 10.1016/j.tecto.2010.05.024
- 1003 Ellis, S., Beaumont, C., & Pfiffner, O. A. (1999). Geodynamic models of crustal-
- 1004 scale episodic tectonic accretion and underplating in subduction zones. *Jour-*
- 1005 *nal of Geophysical Research: Solid Earth*, *104*(B7), 15169–15190. doi: 10.1029/  
1006 1999JB900071
- 1007 Erdős, Z., Huismans, R. S., & van der Beek, P. (2019). Control of increased
- 1008 sedimentation on orogenic fold-and-thrust belt structure – insights into
- 1009 the evolution of the Western Alps. *Solid Earth*, *10*(2), 391–404. doi:
- 1010 10.5194/se-10-391-2019
- 1011 Gerya, T. V., Fossati, D., Cantieni, C., & Seward, D. (2009). Dynamic effects of
- 1012 aseismic ridge subduction: numerical modelling. *European Journal of Mineral-*
- 1013 *ogy*, *21*(3), 649–661. doi: 10.1127/0935-1221/2009/0021-1931
- 1014 Gerya, T. V., & Stöckhert, B. (2002). Exhumation rates of high pressure meta-
- 1015 morphic rocks in subduction channels: The effect of Rheology. *Geophysical Re-*
- 1016 *search Letters*, *29*(8), 1–19. doi: 10.1029/2002TC001406
- 1017 Gerya, T. V., & Stöckhert, B. (2006). Two-dimensional numerical modeling of tec-
- 1018 tonic and metamorphic histories at active continental margins. *International*
- 1019 *Journal of Earth Sciences*, *90*(2), 250–274. doi: 10.1007/s00531-005-0035-9
- 1020 Gerya, T. V., & Yuen, D. A. (2003). Rayleigh-Taylor instabilities from hydration
- 1021 and melting propel ‘cold plumes’ at subduction zones. *Earth and Planetary*
- 1022 *Science Letters*, *212*, 47–62. doi: 10.1016/S0012-821X(03)00265-6
- 1023 Gerya, T. V., Yuen, D. A., & Maresch, W. V. (2004). Thermomechanical modelling
- 1024 of slab detachment. *Earth and Planetary Science Letters*, *226*, 101–116. doi:
- 1025 10.1016/j.epsl.2004.07.02210.1016/j.epsl.2004.07.02210.1016/j.epsl.2004.07.022
- 1026 Glerum, A., Thieulot, C., Fraters, M., Blom, C., & Spakman, W. (2018). Nonlinear
- 1027 viscoplasticity in ASPECT: Benchmarking and applications to subduction.
- 1028 *Solid Earth*, *9*(2), 267–294. doi: 10.5194/se-9-267-2018
- 1029 Gün, E., Pysklywec, R. N., Göğüş, O. H., & Topuz, G. (2022). Terrane geodynam-
- 1030 ics: Evolution on the subduction conveyor from pre-collision to post-collision
- 1031 and implications on tethyan orogeny. *Gondwana Research*, *105*, 399–415. doi:
- 1032 10.1016/j.gr.2021.09.018
- 1033 Heuret, A., Funiciello, F., Faccenna, C., & Lallemand, S. (2007). Plate kinematics,
- 1034 slab shape and back-arc stress: A comparison between laboratory models and
- 1035 current subduction zones. *Earth and Planetary Science Letters*, *256*, 473–483.
- 1036 doi: 10.1016/j.epsl.2007.02.004
- 1037 Hirth, G., & Kohlstedt, D. (2003). Rheology of the upper mantle and the mantle

- wedge: A view from the experimentalists. In *Inside the subduction factory* (pp. 83–105). American Geophysical Union (AGU). doi: 10.1029/138GM06
- Hughes, T. J. R., & Brooks, A. (1982). A theoretical framework for Petrov-Galerkin methods with discontinuous weighting functions: application to the streamline-upwind procedure. *Finite Elements in Fluids*, 4, 47–65.
- Huisman, R. S., & Beaumont, C. (2003). Symmetric and asymmetric lithospheric extension: Relative effects of frictional-plastic and viscous strain softening. *Journal of Geophysical Research: Solid Earth*, 108(B10), 1–22. doi: 10.1029/2002JB002026
- Huisman, R. S., Buitter, S. J. H., & Beaumont, C. (2005). Effect of plastic-viscous layering and strain softening on mode selection during lithospheric extension. *Journal of Geophysical Research: Solid Earth*, 110(B2), 1–17. doi: 10.1029/2004JB003114
- Ismail-Zadeh, A., & Tackley, P. J. (2010). *Computational Methods for Geodynamics*. New York: Cambridge University Press.
- Jarrard, R. D. (1986). Relations Among Subduction Parameters. *Review of Geophysics*, 24(2), 217–284.
- Karato, S.-I. (2008). *Deformation of Earth Materials - An introduction to the rheology of solid Earth*. Cambridge University Press. doi: 10.1017/cbo9780511804892
- Kaus, B. J. P., Mühlhaus, H., & May, D. A. (2010). A stabilization algorithm for geodynamic numerical simulations with a free surface. *Physics of the Earth and Planetary Interiors*. doi: 10.1016/j.pepi.2010.04.007
- Koptev, A., Beniést, A., Gerya, T., Ehlers, T. A., Jolivet, L., & Leroy, S. (2019). Plume-induced breakup of a subducting plate: Microcontinent formation without cessation of the subduction process. *Geophysical Research Letters*, 46(7), 3663–3675. doi: 10.1029/2018GL081295
- Lallemand, S., Heuret, A., & Boutelier, D. (2005). On the relationships between slab dip, back-arc stress, upper plate absolute motion, and crustal nature in subduction zones. *Geochemistry Geophysics Geosystems*, 6(9), 1–18. doi: 10.1029/2005GC000917
- Le Pourhiet, L., May, D. A., Huille, L., Watremez, L., & Leroy, L. (2017). A genetic link between transform and hyper-extended margins. *Earth and Planetary Science Letters*, 465, 184–192. doi: 10.1016/j.epsl.2017.02.043
- Liu, L., Zhang, J., Green, H. W., Jin, Z., & Bozhilov, K. N. (2007). Evidence of former stishovite in metamorphosed sediments, implying subduction to  $\geq 350$  km. *Earth and Planetary Science Letters*, 263(3), 180–191. doi: 10.1016/j.epsl.2007.08.010
- Magni, V., Naliboff, J., Prada, M., & Gaina, C. (2021). Ridge jumps and mantle exhumation in back-arc basins. *Geosciences*, 11(11), 475. doi: 10.3390/geosciences11110475
- Marotta, A. M., Restelli, F., Bollino, A., Regorda, A., & Sabadini, R. (2020). The static and time-dependent signature of ocean-continent and ocean-ocean subduction: the case studies of Sumatra and Mariana complexes. *Geophysical Journal International*, 221(2), 788–825. doi: 10.1093/gji/ggaa029
- Marotta, A. M., Spelta, E., & Rizzetto, C. (2006). Gravity signature of crustal subduction inferred from numerical modelling. *Geophys. J. Int.*, 166, 923–938. doi: 10.1111/j.1365-246X.2006.03058.x
- Molnar, N. E., Cruden, A. R., & Betts, P. G. (2018). Unzipping continents and the birth of microcontinents. *Geology*, 46(5), 451–454. doi: 10.1130/G40021.1
- Müller, R. D., Gaina, C., Roest, W. R., & Hansen, D. L. (2001). A recipe for microcontinent formation. *Geology*, 29(3), 203. doi: 10.1130/0091-7613(2001)029<0203:arfmf>2.0.co;2
- Naliboff, J. B., & Buitter, S. J. H. (2015). Rift reactivation and migration during multiphase extension. *Earth and Planetary Science Letters*, 421, 58–67. doi:

- 1093 <http://dx.doi.org/10.1016/j.epsl.2015.03.050>
- 1094 Naliboff, J. B., Glerum, A., Brune, S., Péron-Pinvidic, G., & Wrona, T. (2020).  
 1095 Development of 3-D Rift Heterogeneity Through Fault Network Evo-  
 1096 lution. *Geophysical Research Letters*, *47*(13), e2019GL086611. doi:  
 1097 10.1029/2019GL086611
- 1098 Nemčok, M., Sinha, S. T., Doré, A. G., Lundin, E. R., Mascle, J., & Rybár, S.  
 1099 (2016). Mechanisms of microcontinent release associated with wrenching-  
 1100 involved continental break-up: a review. *Geological Society, London, Special*  
 1101 *Publications*, *431*(1), 323–359. doi: 10.1144/sp431.14
- 1102 O'Brien, P. J., Zotov, N., Law, R., Khan, M. A., & Jan, M. Q. (2001). Coesite in  
 1103 Himalayan eclogite and implications for models of India-Asia collision. *Geol-*  
 1104 *ogy*, *29*, 435–438. doi: 10.1130/0091-7613(2001)029<0435:CIHEAI>2.0.CO;2
- 1105 Peng, Y., Yu, S., Li, S., Liu, Y., Santosh, M., Lv, P., . . . Liu, Y. (2022). Tectonic  
 1106 erosion and deep subduction in central tibet: Evidence from the discovery of  
 1107 retrograde eclogites in the amdo microcontinent. *Journal of Metamorphic*  
 1108 *Geology*, *40*(9), 1545-1572. doi: 10.1111/jmg.12685
- 1109 Péron-Pinvidic, G., & Manatschal, G. (2010). From microcontinents to extensional  
 1110 allochthons: witnesses of how continents rift and break apart? *Petroleum Geo-*  
 1111 *science*, *16*(3), 189–197. doi: 10.1144/1354-079309-903
- 1112 Petersen, K. D., & Schiffer, C. (2016). Wilson cycle passive margins: Control of oro-  
 1113 genic inheritance on continental breakup. *Gondwana Research*, *39*, 131–144.  
 1114 doi: 10.1016/j.jgr.2016.06.012
- 1115 Polino, R., Dal Piaz, G. V., & Gosso, G. (1990). Tectonic erosion at the Adria  
 1116 margin and accretionary processes for the Cretaceous orogeny of the Alps .  
 1117 *Mémoires de la Société Géologique de France*, *156*, 345–367.
- 1118 Quinquis, M. E. T., & Buiter, S. J. H. (2014). Testing the effects of basic numerical  
 1119 implementations of water migration on models of subduction dynamics. *Solid*  
 1120 *Earth*, *5*(1), 537–555. doi: 10.5194/se-5-537-2014
- 1121 Ranalli, G. (1995). *Rheology of the Earth*. Springer Netherlands.
- 1122 Regorda, A. (2022). *FALCON: a 2D numerical model*. Zenodo. doi: 10.5281/zenodo  
 1123 .7081225
- 1124 Regorda, A., & Roda, M. (2023). *Microcontinent collision: input and dataset vtu*  
 1125 *files*. Zenodo. doi: 10.5281/zenodo.8304780
- 1126 Regorda, A., Roda, M., Marotta, A. M., & Spalla, M. I. (2017). 2-D numerical study  
 1127 of hydrated wedge dynamics from subduction to post-collisional phases. *Geo-*  
 1128 *physical Journal International*, *211*(2), 974–1000. doi: 10.1093/gji/ggx336
- 1129 Regorda, A., Spalla, M. I., Roda, M., Lardeaux, J., & Marotta, A. M. (2021). Meta-  
 1130 morphic Facies and Deformation Fabrics Diagnostic of Subduction: Insights  
 1131 From 2D Numerical Models. *Geochemistry, Geophysics, Geosystems*, *22*(10).  
 1132 doi: 10.1029/2021GC009899
- 1133 Regorda, A., Thieulot, C., van Zelst, I., Erdős, Z., Maia, J., & Buiter, S. (2023).  
 1134 Rifting Venus: Insights From Numerical Modeling. *Journal of Geophysical*  
 1135 *Research: Planets*, *128*(3), e2022JE007588. doi: 10.1029/2022JE007588
- 1136 Roda, M., Marotta, A. M., & Spalla, M. I. (2010). Numerical simulations of an  
 1137 ocean-continent convergent system: Influence of subduction geometry and  
 1138 mantle wedge hydration on crustal recycling. *Geochemistry Geophysics Geosys-*  
 1139 *tems*, *11*(5), 1–21. doi: 10.1029/2009GC003015
- 1140 Roda, M., Marotta, A. M., & Spalla, M. I. (2011). The effects of the overriding  
 1141 plate thermal state on the slab dip in an ocean-continent subduction sys-  
 1142 tem. *Compte Rendu Academie des Sciences Paris*, *343*(5), 323–330. doi:  
 1143 10.1016/j.crte.2011.01.005
- 1144 Roda, M., Spalla, M. I., & Marotta, A. M. (2012). Integration of natural data  
 1145 within a numerical model of ablative subduction: a possible interpretation  
 1146 for the Alpine dynamics of the Austroalpine crust. *Journal of Metamorphic*  
 1147 *Geology*, *30*(9), 973–996. doi: 10.1111/jmg.12000

- 1148 Rolf, T., Capitanio, F. A., & Tackley, P. J. (2018). Constraints on mantle viscos-  
 1149 ity structure from continental drift histories in spherical mantle convection  
 1150 models. *Tectonophysics*, *746*, 339–351. doi: 10.1016/j.tecto.2017.04.031
- 1151 Rosenbaum, G., & Lister, G. S. (2005). The Western Alps from the Jurassic to  
 1152 Oligocene: spatio-temporal constraints and evolutionary reconstructions.  
 1153 *Earth-Science Reviews*, *69*, 281–306. doi: 10.1016/j.earscirev.2004.10.001
- 1154 Salazar-Mora, C. A., Huismans, R. S., Fossen, H., & Egydio-Silva, M. (2018). The  
 1155 Wilson Cycle and Effects of Tectonic Structural Inheritance on Rifted Passive  
 1156 Margin Formation. *Tectonics*, *37*(9), 3085–3101. doi: 10.1029/2018TC004962
- 1157 Schellart, W. P. (2005). Influence of the subducting plate velocity on the geometry  
 1158 of the slab and migration of the subduction hinge. *Earth and Planetary Sci-  
 1159 ence Letters*, *231*, 197–219. doi: 10.1016/j.epsl.2004.12.019
- 1160 Scrutton, R. A. (1976). Microcontinents and their significance. In *Geodynamics:  
 1161 Progress and prospects* (p. 177-189). American Geophysical Union (AGU). doi:  
 1162 10.1029/SP005p0177
- 1163 Sinha, S. T., Nemčok, M., Choudhuri, M., Sinha, N., & Rao, D. P. (2015). The role  
 1164 of break-up localization in microcontinent separation along a strike-slip mar-  
 1165 gin: the east india–elan bank case study. *Geological Society, London, Special  
 1166 Publications*, *431*(1), 95–123. doi: 10.1144/sp431.5
- 1167 Smith, D. C. (1984). Coesite in clinopyroxene in the Caledonides and its implication  
 1168 for geodynamics. *Nature*, *310*, 641–644.
- 1169 Sobolev, N. V., & Shatsky, V. S. (1990). Diamond inclusions in garnets from meta-  
 1170 morphic rocks. *Nature*, *343*, 742–746.
- 1171 Sobolev, S. V., & Babeyko, A. Y. (2005). What drives orogeny in the Andes? *Geol-  
 1172 ogy*, *33*(8), 617–620. doi: 10.1130/G21557.1
- 1173 Spalla, M. I., Lardeaux, J.-M., Dal Piaz, G. V., Gosso, G., & Messiga, B. (1996).  
 1174 Tectonic significance of alpine eclogites. *Journal of Geodynamics*, *21*(3), 257–  
 1175 285. doi: 10.1016/0264-3707(95)00033-X
- 1176 Stein, M., & Ben-Avraham, Z. (2007). Mechanisms of Continental Crust Growth. In  
 1177 G. Schubert (Ed.), *Treatise on geophysics* (pp. 171–195). Amsterdam: Elsevier.  
 1178 doi: 10.1016/B978-044452748-6.00144-9
- 1179 Tao, J., Dai, L., Lou, D., Li, Z.-H., Zhou, S., Liu, Z., ... Li, F. (2020). Accretion of  
 1180 oceanic plateaus at continental margins: Numerical modeling. *Gondwana Re-  
 1181 search*, *81*, 390-402. doi: 10.1016/j.gr.2019.11.015
- 1182 Tetreault, J. L., & Buiter, S. J. H. (2012). Geodynamic models of terrane accretion:  
 1183 Testing the fate of island arcs, oceanic plateaus, and continental fragments in  
 1184 subduction zones. *Journal of Geophysical Research: Solid Earth*, *117*(B8). doi:  
 1185 10.1029/2012JB009316
- 1186 Tetreault, J. L., & Buiter, S. J. H. (2014). Future accreted terranes: a compilation  
 1187 of island arcs, oceanic plateaus, submarine ridges, seamounts, and continental  
 1188 fragments. *Solid Earth*, *5*(2), 1243–1275. doi: 10.5194/se-5-1243-2014
- 1189 Theunissen, T., & Huismans, R. S. (2019). Long-Term Coupling and Feedback  
 1190 Between Tectonics and Surface Processes During Non-Volcanic Rifted Margin  
 1191 Formation. *Journal of Geophysical Research: Solid Earth*, *124*(11), 12323–  
 1192 12347. doi: 10.1029/2018JB017235
- 1193 Thieulot, C. (2011). FANTOM: Two- and three-dimensional numerical modelling of  
 1194 creeping flows for the solution of geological problems. *Physics of the Earth and  
 1195 Planetary Interiors*, *188*(1-2), 47–68. doi: 10.1016/j.pepi.2011.06.011
- 1196 Thieulot, C. (2014). ELEFANT: a user-friendly multipurpose geodynamics code.  
 1197 *Solid Earth Discussions*, *6*(2), 1949–2096. doi: 10.5194/sed-6-1949-2014
- 1198 Thieulot, C., & Bangerth, W. (2022). On the choice of finite element for applications  
 1199 in geodynamics. *Solid Earth*, *13*(1), 229–249. doi: 10.5194/se-13-229-2022
- 1200 van den Broek, J., & Gaina, C. (2020). Microcontinents and continental fragments  
 1201 associated with subduction systems. *Tectonics*, *39*(8), e2020TC006063. doi: 10  
 1202 .1029/2020TC006063

- 1203 van den Broek, J., Magni, V., Gaina, C., & Buitert, S. (2020). The formation of  
 1204 continental fragments in subduction settings: The importance of structural  
 1205 inheritance and subduction system dynamics. *Journal of Geophysical Research: Solid Earth*, *125*(1), e2019JB018370. doi: 10.1029/2019JB018370  
 1206  
 1207 van Zelst, I., Cramer, F., Pusok, A. E., Glerum, A., Dannberg, J., & Thieulot, C.  
 1208 (2022). 101 geodynamic modelling: how to design, interpret, and communi-  
 1209 cate numerical studies of the solid Earth. *Solid Earth*, *13*(3), 583–637. doi:  
 1210 10.5194/se-13-583-2022  
 1211 Vogt, K., & Gerya, T. V. (2014). From oceanic plateaus to allochthonous terranes:  
 1212 Numerical modelling. *Gondwana Research*, *25*(2), 494–508. doi: 10.1016/j.jgr  
 1213 .2012.11.002  
 1214 Wang, H., Agrusta, R., & van Hunen, J. (2015). Advantages of a conservative  
 1215 velocity interpolation (CVI) scheme for particle-in-cell methods with applica-  
 1216 tion in geodynamic modeling. *Geochemistry, Geophysics, Geosystems*, *16*(6),  
 1217 2015–2023. doi: 10.1002/2015GC005824  
 1218 Wang, X., Liou, J. G., & Mao, H. K. (1989). Coesite-bearing eclogite from the  
 1219 Dabie mountains in central China. *Geology*, *17*(12), 1085. doi: 10.1130/0091-  
 1220 -7613(1989)017(1085:cbeftd)2.3.co;2  
 1221 Warren, C. J., Beaumont, C., & Jamieson, R. A. (2008). Modelling tectonic styles  
 1222 and ultra-high pressure (UHP) rock exhumation during the transition from  
 1223 oceanic subduction to continental collision. *Earth and Planetary Science  
 1224 Letters*, *267*, 129–145. doi: 10.1016/j.epsl.2007.11.025  
 1225 Wessel, P., & Smith, W. H. F. (1998). New, improved version of generic mapping  
 1226 tools released. *Eos, Transactions American Geophysical Union*, *79*(47), 579.  
 1227 doi: 10.1029/98EO00426  
 1228 Wessel, P., & Smith, W. M. F. (2001). New improved version of generic mapping  
 1229 tools released. *EOS Transactions of the American Geophysical Union*, *79*,  
 1230 579.  
 1231 Wilks, K. R., & Carter, N. L. (1990). Rheology of some continental lower crustal  
 1232 rocks. *Tectonophysics*, *182*(1-2), 57–77. doi: 10.1016/0040-1951(90)90342-6  
 1233 Wolf, S. G., & Huisman, R. S. (2019). Mountain building or backarc extension  
 1234 in ocean-continent subduction systems: A function of backarc lithospheric  
 1235 strength and absolute plate velocities. *Journal of Geophysical Research: Solid  
 1236 Earth*, *124*(7), 7461–7482. doi: 10.1029/2018JB017171  
 1237 Yan, Z., Chen, L., Zuzva, A. V., Tang, J., Wan, B., & Meng, Q. (2022). The fate  
 1238 of oceanic plateaus: subduction versus accretion. *Geophysical Journal Interna-  
 1239 tional*, *231*(2), 1349–1362. doi: 10.1093/gji/ggac266  
 1240 Yang, S.-H., Li, Z.-H., Gerya, T., Xu, Z.-Q., & Shi, Y.-L. (2018). Dynam-  
 1241 ics of terrane accretion during seaward continental drifting and oceanic  
 1242 subduction: Numerical modeling and implications for the Jurassic crustal  
 1243 growth of the Lhasa terrane, Tibet. *Tectonophysics*, *746*, 212–228. doi:  
 1244 10.1016/j.tecto.2017.07.018  
 1245 Yuan, X. P., Braun, J., Guerit, L., Rouby, D., & Cordonnier, G. (2019). A new  
 1246 efficient method to solve the stream power law model taking into account sed-  
 1247 iment deposition. *Journal of Geophysical Research: Earth Surface*, *124*(6),  
 1248 1346–1365. doi: 10.1029/2018JF004867  
 1249 Yuan, X. P., Braun, J., Guerit, L., Simon, B., Bovy, B., Rouby, D., . . . Jiao, R.  
 1250 (2019). Linking continental erosion to marine sediment transport and de-  
 1251 position: A new implicit and O(n) method for inverse analysis. *Earth and  
 1252 Planetary Science Letters*, *524*, 115728. doi: 10.1016/j.epsl.2019.115728